https://doi.org/10.1016/j.ijmecsci.2021.106659

Modeling of Pitting Damage-induced Ultrasonic Nonlinearity in AL-Whipple Shields of Spacecraft: *Theory, Simulation, and Experimental Validation*

Wuxiong Cao[a,b,c], Lei Xu[d], Zhongqing Su[d], Baojun Pang[a,b], Runqiang Chi[a,b,]*, Lei Wang[e], and Xiaoyu Wang[e,]†

[a] Hypervelocity Impact Research Centre
Harbin Institute of Technology, Harbin 150080, P.R. China

[b] School of Astronautics
Harbin Institute of Technology, Harbin 150080, P.R. China

[c] School of Mechatronics Engineering
Harbin Institute of Technology, Harbin 150080, P.R. China

[d] Department of Mechanical Engineering
The Hong Kong Polytechnic University, Kowloon, 999077, Hong Kong SAR

[e] Beijing Institute of Spacecraft System Engineering, Beijing 100094, P.R. China

Submitted to *International Journal of Mechanical Sciences*
(Initially submitted on 18th January 2021; Revised and resubmitted 8th July 2021)

* To whom correspondence should be addressed. Tel.: +86-139-3613-1193, Fax: +86-0451-8640-2055;
Email: chirq@hit.edu.cn (Prof. Runqiang Chi, *Ph.D.*)

† To whom correspondence should be addressed. Tel.: +86-139-1185-5432;
Email: antlb@163.com (Dr. Xiaoyu Wang, *Ph.D.*)

Abstract

Prevailing but most insidious, pitting damage in the Whipple shield of spacecraft, engendered by a hypervelocity impact (HVI, exceeding 3.0 km/s), is a typical modality of material degradation and lesion in space assets. Featuring multitudinous clustered craters, cracks and diversity of microstructural damages (*e.g.*, dislocation plasticity, micro-voids and cracks) disorderedly scattered over a wide region, pitting damage induces highly complex, mutually-interfering wave scattering, making signal interpretation a daunting task, let alone the quantitative characterization of a pitted region. With this motivation, a dedicated modeling technique is proposed to scrutinize the modulation mechanism of various modalities of pitting damage on the probing ultrasonic waves, based on retrofitted nonlinear constitutive equations by comprehensively considering all nonlinearities originated from different damage sources (*e.g.*, inherent material imperfections, as well as the above HVI-induced intensified plasticity and micro-cracks, *etc*.). On this basis, a quantitative correlation between the nonlinear features (*i.e.*, second harmonics) of ultrasonic waves and the pitting damage severity is established. The modeling technique is experimentally corroborated, and the results demonstrate good consistency in between, revealing that: (1) the proposed modeling approach is feasible to faithfully simulate and precisely evaluate pitting damage-incurred nonlinearities manifested in ultrasonic waves; (2) the ultrasonic nonlinearity intensifies with the increase of pitting damage severity; and (3) the detection sensibility and cumulative effect of second harmonics are related to the “internal resonance” conditions, representing by the excitation frequency. This study yields a structural health monitoring strategy for accurately characterizing pitting-type damage at an embryo stage and surveilling material deterioration progress continuously.

***Keywords*:** pitting damage, hypervelocity impact, finite element modeling, ultrasonic nonlinearity, quantitative characterization

1. Introduction

Pitting damage is a pervasive modality of material lesion in engineering structures in harsh service environment. Amongst numerous examples are electrical pitting in rolling bearings [1,2], pits in wind turbine blades [3], pitting corrosion in maritime structures or pipelines [4-6], and pitting craters in on-orbit spacecraft induced by micrometeoroids/orbital debris (MMOD) hypervelocity impact (HVI) [7,8], as typified in Fig. 1. Degradative and deteriorative changes in material microstructures induced by pitting damage, usually initiated at an unperceivable level but progressing at an alarming speed, can fairly compromise structural integrity, durability and performance, and without timely awareness lead to fragmentation and even failure of the entire system. This has entailed early perceiving of pitting damage and accurate assessment of its severity, on which basis follow-up remedial actions can be implemented, whereby the risk of consequent structural failure might be minimized. However, it is an extremely challenging and daunting task to characterize pitting damage, because of its highly specific manifestation – multitudinous small-scale craters and cracks disorderedly clustered over a wide region ("*pitted region*" hereinafter), accompanied with various microstructural defects (*e.g.*, dislocation plasticity, micro-voids and cracks) [9].

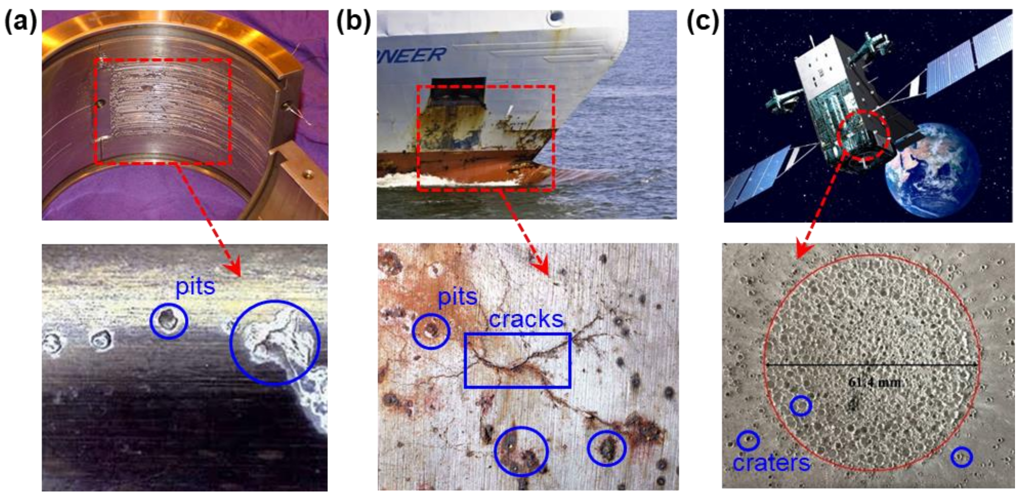

Fig. 1. (a) Electrical pitting in rolling bearings; (b) pitting corrosion in maritime structure [5]; and (c) pitting craters in spacecraft caused by MMOD [8].

To characterize pitting damage (or *pitted region*), a diversity of structural health monitoring (SHM) and nondestructive evaluation (NDE) techniques [10-16] have been developed and employed, for instance ultrasonic wave, eddy-current, thermography, resonance imagery, to name a few. Representatively, Zhang *et al* [8] statistically calculated the diameters and depths of all craters larger than 1 mm in the pitted region, as well as the region size, using a three-dimensional (3D) scanner. Takashi *et al* [13] imaged the cavitation (or pitting) damage region, containing a constellation of micro-pits generated by large numbers of magnetic impacts, by employing a nonlinear ultrasonic imaging approach with resonance and non-resonance modes, respectively. Bao *et al* [14] proposed a transmitter beamforming and weighted image fusion-based multiple signal classification (MUSIC) algorithm, in conjunction with the use of a dual sensor arrays, to quantify the severity of pitting corrosion (mainly the average depth) and obtained its localization. Francesco *et al* [15] presented a guided ultrasonic wave (GUW)-based tomography method for achieving the localization of corrosion damage. Rao *et al* [16] on-line continuously monitored the thickness loss of a plate-like structure undergoing corrosion, using a GUW-based self-designed piezoelectric transducer array.

However, the above-mentioned approaches generally treat the whole pitting-damaged region as singular damage or area, ignoring individual damages (*e.g.*, craters and cracks) within this pitted region *de facto*, so that isolation and interpretation of ultrasonic waves scattered by individual damages could be avoided. Such a compromise restricts the detection of pitting-type damage at a qualitative or quasi-quantitative level – indicating only the presence, location, approximate periphery, and average severity of a pitted region, and failing to quantitatively evaluate the severity in different position of a pitted region, as well as interpret the modulation mechanism of various modalities of pitting damage on the probing GUWs.

Targeting quantitative characterization of the highly complex pitting, existing interrogation methods are confronted with the following bottlenecks:

(1) various types of damage sources are densely clustered in the pitted region. When traversing this region, the probing GUWs are severely mixed and overlapped due to the scattering or distortion caused by the large number of damages with sizes comparable to the wavelength of probing GUWs, demonstrating high complexity of signal appearance and obfuscation of damage-related linear features (*e.g.*, wave reflection, transmission and scattering, energy transfer, mode conversion and time-of-flight);

(2) or, if the sizes of damages are much smaller than the wavelength of probing GUWs, no remarkable wave-scattering phenomena as clarified in (1) will be induced, and this will lead to absence of discernable changes in the above-mentioned linear features. Consequently, these microstructural damages may be underestimated or overlooked;

(3) these damages, acting as nonlinear sources *per se*, jointly lead to the distortion of the probing GUWs, making separately interpret the contribution of each damage source to the generation of ultrasonic nonlinearity a daunting task in experimental measurements.

To circumvent the above deficiency, nonlinear ultrasonic waves (NUWs) have been studied and exploited intensively, in accordance with the fact that pitting damage can induce exceptional ultrasonic nonlinearity which is more sensitive than their linear counterpart to small-sized damage [17-23]. In addition, theoretical derivation and numerical modelling of NUWs propagating in damaged structure are performed, providing a physical insight into the nonlinear ultrasonic responses against various types of damage sources, separately, such as micro-cracks [18,19], de-bonding at adhesive joints [24,25], dislocation plasticity [26-29], and inherent material imperfections [30-33]. Representatively, Chillara *et al* [26] numerically canvassed the contributions of material and geometric nonlinearities, and third-order elastic constants (TOECs) to the generation of high-order harmonics. Cantrell *et al* [27] proposed theoretical models to quantified the effect of dislocation plasticity, vacancy and micro-crack on ultrasonic nonlinearities. Zhu *et al* [28,29] examined the nonlinear ultrasonic responses on plastic deformation and dislocation evolution via numerical simulations. Wang *et al* [34,35] analytically and numerically illuminated the generation of contact acoustic nonlinearity (CAN) by modeling 2D and 3D “breathing” cracks, respectively, and predicted the crack-induced wave fields. Zhao *et al* [36,37] investigated the modulation mechanism of randomly distributed micro-cracks on the propagating GUWs using numerical simulations, establishing a quantitative relationship between the ultrasonic nonlinear features and the characteristics of micro-cracks.

Even though, modeling of the pitting-damaged structure in finite element method (FEM) are difficult due to the numerous and highly complex modalities of microstructural damages, acting as the nonlinear sources *per se*. Therefore, it is hitherto still a paramount challenge to interpret the modulation mechanism of all possible nonlinear sources attribute of pitting damage on the probing NUWs, let alone to quantitatively and precisely characterize its severity. In recognition of this, a dedicated theoretical modeling technique is developed, combining the contributions of various microstructural defects to ultrasonic nonlinearity with the retrofitted nonlinear constitutive equations, to scrutinize the generation and accumulation mechanism of high-order harmonics in the propagating NUWs for both intact and pitting-damaged plates. Finite element (FE) simulation is then conducted for proof-of-concept validation, in which identified sources of nonlinearities are comprehensively considered to describe their corresponding nonlinear ultrasonic responses. As a practical application, the proposed method is utilized to quantitatively characterize HVI-induced pitting damage in AL-Whipple shields of spacecraft.

2. Modulation Mechanism of Pitting Damage on a Probing GUW ─ Theoretical Modeling

2.1. Principle of Approach

For a plate-like waveguide bearing HVI-induced pitting damage, morphological and metallographic analyses indicate that in a typical pitted region, besides hundreds of macroscopic craters and cracks, a diversity of microscopic changes, such as micro-voids and cracks, dislocations, shock hardening and recrystallized sub-grains, co-exist in a wide area, as displayed in our previous works (Fig. 2) [9, 38]. These microstructural defects are thought to be the sources of ultrasonic nonlinearity for propagating GUWs. According to the damage mechanism of debris cloud in the plate-like waveguide [9], non-uniform plastic deformation occurs in the relative wide-scale pitted region, which is relatively higher near the damage center, and decreasing sharply away from the center, leading to the change in the nonlinear material properties.

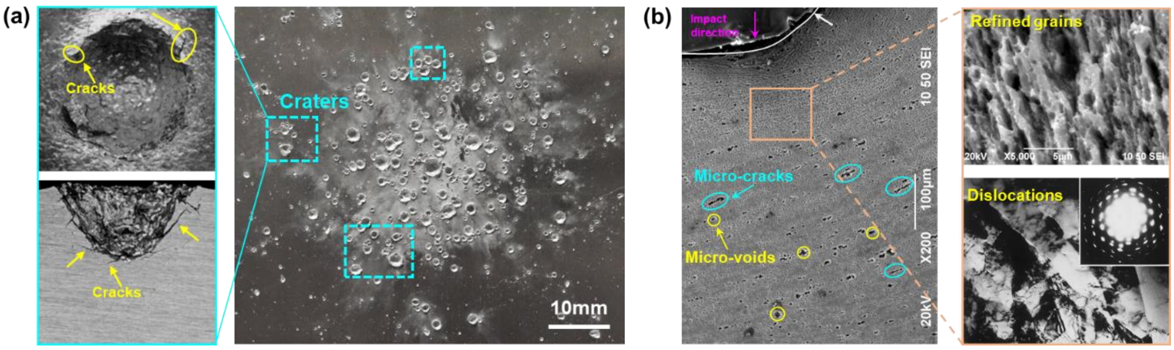

Fig. 2. Typical modalities of HVI-induced pitting damage: (a) macro-damage on the surface, including pitting craters and surface cracks; and (b) microstructure underneath a pitted crater, showing dislocation substructures, sub-grains and micro-cracks/voids. [9,38].

There are two kinds of physical mechanisms in the generation of second harmonics for the pitting damaged waveguide. One is the nonlinear elastic response of material, the other is microstructural defects triggered CAN. A pitted region introduces plastic deformation and consequently plastic strains to polycrystalline structures of the material [27-29], which in turn contributes to the enhancement of material nonlinearity in this damaged region, in particular the periphery of pitting craters. In addition, the probing GUW will be modulated or distorted by the micro-voids and cracks when traversing the pitted region, leading to partial wave energy transfer from the fundamental (excitation) frequency to fractional or integer multiple of the fundamental frequency, so-called sub-harmonics or super-harmonics generation [18-21], thereby triggering CAN [34,35], as illustrated schematically in Fig. 3. With such a premise, the severity of HVI-induced pitting damage is correlated to the different degrees of collective manifestation of plastic strain in the material, which can be calibrated with the amplitude of generated second harmonics – one of the key nonlinear features of GUWs. This interaction of a propagating GUW with various modalities of pitting damage occurs at the microscopic level, and the generated nonlinear features are more sensitive to microstructural damages (*e.g.*, dislocation plasticity and micro-cracks and voids) in a pitted region, compared with their linear features.

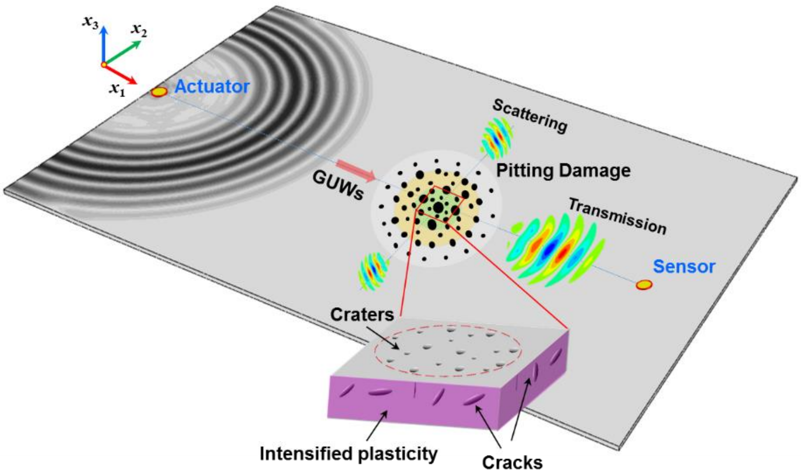

Fig. 3. Illustration of wave propagation in a plate-like waveguide containing pitting damage.

In virtue of their sensitivity to evaluate microstructural degradation, including inherent material imperfections, dislocation plasticity, micro-voids and cracks [22,23,27], these harmonics are regarded as appealing nonlinear features for NUWs-based micro-scale damage evaluation. Amongst which, the second harmonic is pervasively applied because of its relative convenience and feasibility in acquisition when compared with other order harmonics. To gain a deep insight into the generation and accumulation mechanism of second harmonic, and use it for accurate characterization of pitting damage, a dedicated analytical modeling approach is proposed. In this model, three identified types of nonlinear sources are considered, including the inherent material imperfections (*e.g.*, precipitates, vacancies, and lattices anharmonicity) [23,39], pitting damage-induced localized plasticity (*e.g.*, dislocation substructures) [27,28] and material lesion (*e.g.*, micro-cracks and voids) [22,23].

2.2. Fundamental Equations of Nonlinear Elastodynamics

Considering an isotropic medium neglecting attenuation and dispersion, the wave motion equation for the longitudinal wave in the Lagrangian coordinate is expressed as [28,40]

$$\rho_0 \frac{\partial^2 u_i}{\partial t} = \frac{\partial \sigma_{ij}}{\partial x_j}, \tag{1}$$

where ρ_0 denotes the mass density, u_i the particle displacement vector, t the time, σ_{ij} the stress tensor, and x_j the Lagrangian coordinate in any direction (as shown in Fig. 3). The stress tensor in a nonlinear medium can be expanded in terms of the displacement gradients as (assuming no initial stress) [41,42]

$$\sigma_{ij} = C_{ijkl} \frac{\partial u_k}{\partial x_l} + 1/2\, M_{ijklmn} \frac{\partial u_m}{\partial x_n} \frac{\partial u_k}{\partial x_l} + \cdots, \tag{2}$$

where

$$M_{ijklmn} = C_{ijklmn} + C_{ijln}\delta_{km} + C_{jnkl}\delta_{im} + C_{jlmn}\delta_{ik},$$
$$C_{ijklmn} = \frac{1}{2}\mathcal{A}(\delta_{ik}I_{jlmn} + \delta_{il}I_{jkmn} + \delta_{jk}I_{ilmn} + \delta_{jl}I_{ikmn}) + 2\mathcal{B}(\delta_{ij}I_{klmn} + \delta_{kl}I_{mnij} + \delta_{mn}I_{ijkl}) + 2\mathcal{C}\delta_{ij}\delta_{kl}\delta_{mn}. \quad (3)$$

In the above, $\partial u_m / \partial x_n$ and $\partial u_k / \partial x_l$ denote the strain tensors. C_{ijkl} is the second-order elastic (SOE) tensor determined by Lamé constant λ and μ. M_{ijklmn} signifies a tensor owing to the intrinsic material nonlinearity (IMN) and geometric (or convective) nonlinearity (GMN) [28,39], simultaneously. The former refers to the inherent material imperfections (leading to crystal vibrations in a metallic medium that do not follow the simple harmonic motion), described using the third-order elastic (TOE) tensor C_{ijklmn}, which is directly related to three TOECs, *i.e.*, $\mathcal{A}$, $\mathcal{B}$ and $\mathcal{C}$ (referring to the previous literature [30]). While the latter attributes to the mathematic transformation of wave motion equation from Eulerian (spatial) to Lagrangian (material) coordinates during analytical derivation, which can be addressed via the last three terms of M_{ijklmn}. δ_{ij} and such in similar forms are the Kronecker deltas. I_{ijkl} and such in similar forms are the fourth-order identity tensors.

Assuming that GUWs propagate along the $[100]$ direction of a cubic crystal, the SOECs and TOECs in Eqs. (2) and (3) can be given as $C_{1111} = \lambda + 2\mu$ and $C_{111111} = 2\mathcal{A} + 6\mathcal{B} + 2\mathcal{C}$, respectively [43], Eq. (2) can then be described as

$$\rho_0 \frac{\partial^2 u}{\partial t} = C_{1111}\frac{\partial^2 u}{\partial x_1^2} + (3C_{1111} + C_{111111})\frac{\partial u}{\partial x_1}\frac{\partial^2 u}{\partial x_1^2}, \quad (4)$$

Based on the perturbation theory, the above equation can be solved and the total displacement field u is represented as [41]

$$u = u^{\omega} + u^{2\omega}, \tag{5}$$

where ω represents the angular frequency of a probing GUW. $u^{2\omega}$ denotes the secondary displacement field, which is much smaller than the fundamental displacement field u^{ω} (or initially excited wave). Assuming that an initially pure sinusoidal disturbance ($u^{\omega} = A^{\omega} \cdot \sin(\kappa x_1 - \omega t)$) is excited at $x_1 = 0$ (as shown in Fig. 3), then the perturbation solution of Eq. (5) can be obtained as [44]

$$u = A^{\omega} \cdot \sin(\kappa x_1 - \omega t) - \frac{3C_{1111} + C_{111111}}{C_{1111}} \cdot \frac{(A^{\omega})^2 \kappa^2 x_1}{8} \cdot \cos 2(\kappa x_1 - \omega t), \tag{6}$$

where κ and A^{ω} signify the wavenumber and measured amplitude of fundamental wave, respectively. The coefficient in front of the second term is $-[(3C_{1111} + C_{111111}) / 8C_{1111}](A^{\omega})^2 \kappa^2 x$, the measured amplitude of second harmonics (denoted by $A^{2\omega}$). By simply rearranging these amplitude terms, the IMN for an intact medium can be determined in terms of the measured quantities

$$\beta_{mat} = \frac{8}{\kappa^2 x_1} \cdot \frac{A^{2\omega}}{(A^{\omega})^2} = -\frac{3C_{1111} + C_{111111}}{C_{1111}} \propto 3 + \frac{2\mathcal{A} + 6\mathcal{B} + 2\mathcal{C}}{\lambda + 2\mu}, \tag{7}$$

Obviously, the variation of β_{mat} is ascribed to both the SOECs (*i.e.*, λ and μ) and TOECs (*i.e.*, $\mathcal{A}$, $\mathcal{B}$ and $\mathcal{C}$). It is well known that the SOECs change very little, therefore, it is the TOECs which dominate the IMN in both the analytical and numerical models [29,43].

Based on the above analysis, it is found that the amplitude of second harmonics is a direct measure of the ultrasonic nonlinearity, and then it is vital important to gain an insight into the second harmonic generation in GUW propagation. To obtain the second harmonic field $u^{2\omega}(x_3, x_1)$ of a propagating GUW in Eq. (5), both perturbation approximation and modal expansion analysis approach are recalled, which can then be written as [45]

$$u^{2\omega}(x_3, x_1) = \frac{1}{2}\sum_{m}^{\infty} A_m^{2\omega}(x_1) u_m^{2\omega}(x_3) e^{-i2\omega t} + c.c., \tag{8}$$

where $u_m^{2\omega}(x_3)$ represents the displacement field function (or velocity vector). $c.c.$ is the complex conjugates. The modal amplitude of second harmonics $A_m^{2\omega}(x_1)$ is used to determine the contribution of m^{th} second harmonics in the mode expansion. The solution of $A_m^{2\omega}(x_1)$ in Eq. (8) with the source condition $u^{2\omega}(x_3, x_1) = 0$ at $x_1 = 0$ is given as

$$A_m^{2\omega}(x_1) = \bar{A}_m^{2\omega}(x_1)\, \mathrm{e}^{i(2\kappa)x_1} - \bar{A}_m^{2\omega}(0)\, \mathrm{e}^{i\kappa_n^* x_1}, \tag{9}$$

where κ_n^* signifies the complex conjugate of the wavenumber at 2ω. $\bar{A}_m^{2\omega}(x_1)$ takes the form

$$\bar{A}_m^{2\omega}(x_1) = \begin{cases} \dfrac{i(f_n^{vol} + f_n^{surf})}{4P_{mn}(\kappa_n^* - 2\kappa)}, & \text{if } \kappa_n^* \neq 2\kappa \text{ (asymchronism)}, \\[2ex] \dfrac{(f_n^{vol} + f_n^{surf})}{4P_{mn}} \cdot x_1, & \text{if } \kappa_n^* = 2\kappa \text{ (synchronism)}. \end{cases} \tag{10}$$

In the above, P_{mn} is the complex power flux of an m^{th} mode in direction x_1. f_n^{vol} and f_n^{surf} respectively denote the external driving force (*i.e.*, power flux) for second harmonics generated through the volume force and surface traction, due to the propagation of fundamental waves.

Assuming that a GUW is transmitted at the location $x_1 = 0$, then the amplitude of m^{th} second harmonics is defined as [46]

$$A_m^{2\omega}(x_1) = \frac{f_n^{vol}(x_1) + f_n^{surf}(x_1)}{4P_{mn}} \cdot \frac{c_p^{\omega} c_p^{2\omega}}{\omega(c_p^{2\omega} - c_p^{\omega})} \cdot \sin\left(\frac{\omega(c_p^{2\omega} - c_p^{\omega})}{c_p^{\omega} c_p^{2\omega}} \cdot x_1\right), \tag{11}$$

where c_p^{ω} and $c_p^{2\omega}$ denote the phase velocities of fundamental and secondary waves, respectively. Regarding to a plate-like structure, GUWs are multimodal and dispersive, which can be depicted as [41]

$$\frac{\tanh(0.5qh)}{\tanh(0.5ph)} = -\left[\frac{4\kappa^2 pq}{(q^2-\kappa^2)^2}\right]^{\pm 1}, \tag{12}$$

where the +1 is for the symmetric modes, while -1 is for the antisymmetric modes. h denotes the plate thickness. In the Eq. (12), $p = \sqrt{(\omega / c_L)^2 - \kappa^2}$ and $q = \sqrt{(\omega / c_T)^2 - \kappa^2}$. Phase and group velocities can then be calculated using the Eq. (12) and the parameters in Table 2, as demonstrated in Fig. 4. The former is the propagation velocity of the phase at a specific frequency, while the latter is the velocity at which the energy of a wave travels.

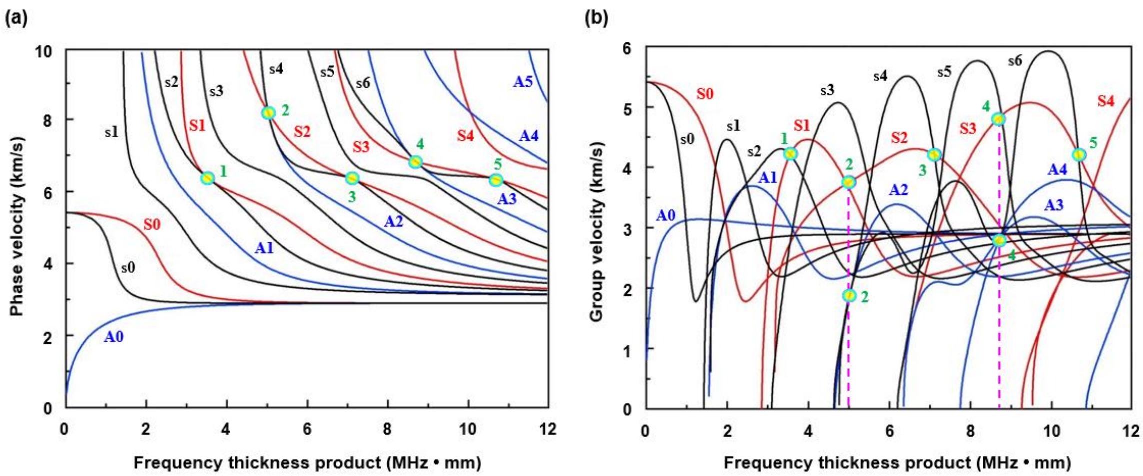

Fig. 4. Dispersion curves for a 1 mm-thick Al-7075 plate: (a) phase velocity; and (b) group velocity. (red and dark lines represent the fundamental and secondary symmetric modes, denoting by S(i) and s(i) (i=0,1,…,6), respectively)[46].

Table 1. Material parameters of Al-7075 [30]

	TOECs			E (GPa)	υ	ρ (kg/m³)	c_L (m/s)	c_T (m/s)	λ (GPa)	μ (GPa)
	$\alpha\mathcal{A}$ (GPa)	$\alpha\mathcal{B}$ (GPa)	$\alpha\mathcal{C}$ (GPa)							
Intact (α=1)	-351.2	-149.4	-102.8	73.1	0.33	2758	6373	3146	55.27	25.95

In the case of $\kappa_n^* = 2\kappa$, which denotes the phase-velocity matching ($c_p^{\omega} = c_p^{2\omega}$, as marked by solid circles in Fig. 4(a)), if the external power flux from fundamental mode to second harmonics is not zero ($f_n^{vol} + f_n^{surf} \neq 0$), $A_m^{2\omega}(x_1)$ will increase linearly (or grow cumulatively) against the propagation distance x_1. This phenomenon is known as the "*internal resonance*" , requiring two conditions: (1) *phase-velocity matching*: $c_p^{\omega} = c_p^{2\omega}$ or $\kappa_n^* = 2\kappa$; (2) *non-zero power flux*: $f_n^{vol} + f_n^{surf} \neq 0$.

Regarding the mode pairs with phase mis-matching ($c_p^{\omega} \neq c_p^{2\omega}$ or $\kappa_n^* \neq 2\kappa$) and non-zero power flux ($f_n^{vol} + f_n^{surf} \neq 0$), $A_m^{2\omega}(x_1)$ remains bounded and oscillates with a spatial periodicity $(x_1)_n$, which can be defined as [30]

$$(x_1)_n = \frac{2\pi}{|\kappa_n - 2\kappa|} = \frac{\pi}{2\omega} \frac{c_p^{\omega} c_p^{2\omega}}{\left|c_p^{2\omega} - c_p^{\omega}\right|}, \quad (13)$$

where the maximum amplitude of $A_m^{2\omega}(x_1)$ can be obtained. Note that $(x_1)_n$ is dependent on the angular frequency and the phase velocities of the fundamental and secondary modes. Considering the dispersive nature of GUWs, the internal resonance conditions (representing by the phase velocity) can be satisfied only at finite excitation frequencies, restricting the practical implementation of damage evaluation.

2.3. Nonlinearity Disturbance in Probing GUWs Due to Pitting Damage

2.3.1. Plasticity-driven Material Nonlinearity

Regarding a pitting-damaged region undergoing plastic deformation, the sub-grains, dislocations, shock hardening, *etc*., together result in enhancement of material plasticity, which could be a source of nonlinearity for the GUWs propagation. Typically, plastic damage-induced ultrasonic nonlinearity is predominantly owed to dislocation evolutions in materials [27-29]. The physical mechanism between the plastic deformation and the probing wave is analogous to that of the inherent material imperfections, which can be described via the retrofitted nonlinear stress-strain constitutive equation. Assuming that a small oscillatory stress $\Delta\sigma$ produced by a probing GUW is superimposed on the initial residual or internal longitudinal stress σ_0, the dislocation will further glide leading to additional strain $\Delta\varepsilon$. Note that both lattice abnormality and dislocation contribute to $\Delta\varepsilon$. The nonlinear stress-strain equation is then derived as [29]

$$\Delta\sigma_{ij} = \overline{C}_{ijkl} \cdot \Delta\varepsilon_{kl} + \frac{1}{2} \cdot \overline{M}_{ijklmn} \cdot \Delta\varepsilon_{mn}\Delta\varepsilon_{kl} + \cdots, \tag{14}$$

where

$$\overline{C}_{ijkl} = \left[\frac{1}{C_{ijkl}} + \frac{2}{3} \cdot \frac{(1-v)}{(1+vf_s-2vf_e)} \cdot \frac{\Omega\rho_{dis}L_{dis}^2 R}{\mu} \right]^{-1},$$
$$\overline{M}_{ijklmn} = \frac{-2\left[-\frac{1}{2} \cdot \frac{M_{ijklmn}}{(C_{ijkl})^3} + \frac{12}{5} \cdot \left(\frac{1-v}{1+vf_s-2vf_e} \right)^3 \cdot \frac{\Omega\rho_{dis}L_{dis}^4 R^3}{\mu^3 b^2} \cdot \sigma_0 \right]}{\left[\frac{1}{C_{ijkl}} + \frac{2}{3} \cdot \frac{(1-v)}{(1+vf_s-2vf_e)} \cdot \frac{\Omega\rho_{dis}L_{dis}^2 R}{\mu} \right]^3}. \tag{15}$$

In the above, v signifies the Poisson's ratio, b the absolute value of Burgers vector (assumed to be 0.286 nm). ρ_{dis} and L_{dis} are the dislocation density and length, respectively. The conversion factor Ω and the resolving shear factor R are assumed to be 0.33. f_s and f_e respectively denote the fractions of edge and screw dislocations. $\overline{C}_{ijkl}$ and $\overline{M}_{ijklmn}$ are modified by pitting damage-induced dislocation substructures from their initial values, C_{ijkl} and M_{ijklmn}. Therefore, this modified constructive equation, *i.e.*, Eq. (14), can be embedded into the following numerical modeling to analyze the nonlinear ultrasonic response in the plastically deformed materials.

In contrast to β_{mat}, another ultrasonic nonlinearity index β_{dis} is constructed to reflect the intensification of localized plasticity-driven material nonlinearity (PMN) in the pitted region. Accordingly, the total ultrasonic nonlinearities caused by dislocations and lattice abnormality can be expressed as

$$\beta_{mat}+\beta_{dis}=-\frac{\overline{M}_{ijklmn}}{\overline{C}_{ijkl}}=\frac{-\dfrac{M_{ijklmn}}{(C_{ijkl})^3}+\dfrac{24}{5}\cdot\left(\dfrac{1-v}{1+vf_s-2vf_e}\right)^3\cdot\dfrac{\Omega\rho_{dis}L_{dis}^4R^3}{\mu^3b^2}\cdot\sigma_0}{\left[\dfrac{1}{C_{ijkl}}+\dfrac{2}{3}\cdot\dfrac{(1-v)}{(1+vf_s-2vf_e)}\cdot\dfrac{\Omega\rho_{dis}L_{dis}^2R}{\mu}\right]^2}, \qquad (16)$$

It is apparent that the localized plastic deformation incurred by radiation, fatigue, shock hardening and thermal aging, *etc*., will lead to the increasing of both SOECs and TOECs. In the above Eq. (16), the term $2(1-v)\Omega\rho_{dis}L_{dis}^2R(1+vf_s-2vf_e)^{-1}/3\mu$ is generally much smaller than $1/C_{ijkl}$, which can be ignored, and the C_{ijkl} usually changes very little [29]. Therefore, it is the TOECs which dominate the increase of nonlinearity parameter. For the convenience and feasibility of modeling, the intensification of material plasticity is assumed to be uniformly distributed and gradually increase with the enhancement of the damage severity. Accordingly, the material nonlinearity of the pitted region, including the IMN and PMN can be described via the increasing TOECs (*i.e.*, $\alpha\mathcal{A}$, $\alpha\mathcal{B}$ and $\alpha\mathcal{C}$, α is the scale factor) in both the analytical and numerical models, and their values are set according to previous literatures[30-33]. The change in nonlinearity parameter due to dislocation is then written as

$$\begin{aligned} \beta_{dis} &= \frac{24}{5}\cdot\left(\frac{1-v}{1+vf_s-2vf_e}\right)^3\cdot\frac{\Omega\rho_{dis}L_{dis}^4R^3(C_{ijkl})^2}{\mu^3b^2}\cdot\sigma_0-\frac{M_{ijklmn}}{C_{ijkl}}-\beta_{mat} \\ &= \frac{24}{5}\cdot\left(\frac{1-v}{1+vf_s-2vf_e}\right)^3\cdot\frac{\Omega\rho_{dis}L_{dis}^4R^3(C_{1111})^2}{\mu^3b^2}\cdot\sigma_0, \end{aligned} \tag{17}$$

which can be simplified to

$$\beta_{dis} \propto \rho_{dis}L_{dis}^4\sigma_0. \tag{18}$$

In the above, the β_{dis} is positively related to the dislocation density and length. As discussed in our previous work [9], with the enhancement of pitting damage, the dislocation density of material increases, and thus leading to a higher β_{dis} . Generally, this PMN engendered by the pitting damage imposes significant effect on propagating GUWs more than the IMN does.

2.3.2. Micro-cracks Induced CAN

CAN is generated mainly by micro-voids/cracks whose opening size are smaller than the particle displacement. Physically, when the ultrasonic waves reach an imperfect contact interface, interaction between micro-cracks and propagating GUWs embraces two alternative stages: (1) crack closing during the compression stage, the effective local elastic moduli of material are considered to be same with that of the continuous material because that the crack becomes tightly closed, in which GUW propagation remains unchanged without distortion and the compressional part of the waves can penetrate it; and (2) crack opening during the tension stage, the local elastic moduli of material are remarkably weakened, corresponding to a discontinuous structure with fully opened cracks, and their tensile part cannot penetrate it, which triggers wave scattering and mode conversion. Thus, after penetrating the interface, the waves become nearly half-wave rectification, which means they have obvious nonlinearity. This parametric modulation phenomenon of quasi-linear material is generally induced by the stress-dependent interfacial stiffness at cracks – called "*breathing crack*". When the cracks entirely open or close, no CAN occurs. Due to localized residual stress in the material, micro-cracks in a typical pitted region are partially closed, then the interaction between the probing GUWs and cracks gives rise to generation of CAN via "breathing" manner, which can be much higher than the IMN.

Micro-cracks induced "breathing" behavior will introduce ultrasonic nonlinearity to the scattered waves, acting as a secondary wave source at the location of micro-crack – namely "*crack-induced secondary source*" (*CISS* hereinafter) [34,35]. The *CISS* at crack is referred as a concentrated force whose amplitude is determined via integration of the *CISS* over the crack surface, as

$$\overrightarrow{CISS}^{open} = \int_{Crack\ surface} -\tilde{\sigma}^{inc} \cdot \vec{x}_1 ds, \qquad (19)$$

where $\tilde{\sigma}^{inc}$ signifies the stress tensor of probing GUWs. $\vec{x}_1$ is the direction vector. $\overrightarrow{CISS}^{open}$ represents the *CISS* generated during crack opening.

The *CISS*, manifesting time-dependent traits, occurs during crack opening and disappears otherwise. To reflect the above periodical characteristic of the "breathing" behavior, an indicator function $f(t)$ is introduced to modulate $\overrightarrow{CISS}^{bre}$, as

$$\overrightarrow{CISS}^{bre} = \overrightarrow{CISS}^{open} \cdot e^{i\omega t} \cdot f(t), \qquad (20)$$

where

$$f(t)=\begin{cases}1, & t_{open}<t<t_{close}\\ 0, & t_{close}<t<t_{open}+T,\end{cases} \tag{21}$$
$$t_{close}=t_{open}+T/2.$$

In Eq. (20), $\overrightarrow{CISS}^{bre}$ denotes the modulated *CISS* attributed to the "breathing" behavior. t_{open} signifies the moment when crack opens, and t_{close} the moment when crack closes, T the duration of a cycle for a propagating GUW. The spectrum of $\overrightarrow{CISS}^{bre}$ for each high-order harmonic can be ascertained via the Eqs. (20) and (21), with the acquired modal amplitude of second harmonic ($A^{2\omega}$), $\overrightarrow{CISS}^{bre}$ at 2ω can be depicted as

$$\overrightarrow{CISS}^{bre-2\omega}=A^{2\omega}\cdot\overrightarrow{CISS}^{open}\cdot e^{i2\omega t}, \tag{22}$$

In accordance with the Eq. (22), the in-plane displacement ($U_m^{S-2\omega}$) of *CISS*-induced m^{th}-order symmetric modes at 2ω can be ascertained as [34,35]

$$U_m^{S-2\omega}=A_m^{S-2\omega}u_m^{S-2\omega}(x_3)\left[H_0^2(k_m^{2\omega}r)-\frac{1}{k_m r}H_1^2(k_m^{2\omega}r)\right], \tag{23}$$

where

$$A_m^{S-2\omega}=\frac{k_m^{2\omega}}{4i}\frac{2CISS_{in}^{bre-2\omega}\cdot u_m^{S-2\omega}(0)}{P_{mm}^S}. \tag{24}$$

In the above, $u_m^{S-2\omega}(x_3)$ is a function of x_3 (subscript m signifying m^{th} order, and superscript S defining symmetric modes), denoting the in-plane displacement. $H^2(\square)$ is the second-order Hankel function. $\kappa_m^{2\omega}$ represents the wavenumber at 2ω, r the distance between crack and sensor (see Fig. 3). $A_m^{S-2\omega}$ signifies micro-crack induced second-order displacement field at 2ω, i the imaginary unit. P_{mm}^{S} is the energy carried by the probing GUW. $u_m^S(0)$ is the in-plane displacement of GUWs at mid-plane. $CISS_{in}^{bre-2\omega}$ denotes the in-plane component of $\overrightarrow{CISS}^{bre-2\omega}$. It is noteworthy that the generation of second harmonics in GUWs propagating in the pitted region with micro-cracks attributes to $\overrightarrow{CISS}^{bre-2\omega}$, with which the ultrasonic nonlinearity (*i.e.*, CAN) is intensified.

2.4. Effect of Micro-cracks Distribution on Nonlinearity

As photographed in Fig. 2, cracks are randomly distributed at the surface of the pitted region, on the periphery of the pitted craters, and in the internal microstructure. This micro-cracking damage can weaken the local mechanical properties (*e.g.*, Young's modulus E, Poisson's ratio ν, *etc*.) of the pitted region, then the effective elastic moduli can be expressed as [47]

$$\begin{aligned}
\overline{E}_c &= E\cdot\left[1+\frac{16(1-\nu_D^2)(10-3\nu_D)V_{crack}}{45(2-\nu_D)}\frac{E}{E_D}\right]^{-1},\\
\overline{G}_c &= G\cdot\left[1+\frac{32(1-\nu_D^2)(5-\nu_D)V_{crack}}{45(2-\nu_D)(1+\nu)}\frac{E}{E_D}\right]^{-1},\\
\overline{\nu}_c &= (\nu+1)\frac{\overline{E}_c}{E}\frac{G}{\overline{G}_c}-1,
\end{aligned} \tag{25}$$

where $\overline{E}_c$, $\overline{G}_c$, and $\overline{\nu}_c$ respectively denote effective Young's modulus, shear modulus, and Poisson's ratio. V_{crack} signifies the crack density, G the pristine shear modulus. E_D and ν_D are the function of pristine E and ν, respectively. Accordingly, it is obviously that the elastic moduli of the pitted region decrease with the increase of crack density.

On top of the crack density, the location of micro-cracking layer along the thickness direction (x_3) also affect the mechanical properties of medium. Assuming that numerous micro-cracks are uniformly distributed in a layer with a thickness of h_2, and the distance between this layer and the bottom and top surfaces of the plate are h_1 and h_3, respectively, as shown in Fig. 5. Therefore, the effective elastic moduli of this micro-cracking layer can be given as $\bar{E}_c$ and $\bar{v}_c$, and other two layers without cracks remain the pristine E and v. Based on equivalent bending principle, the effective Poisson's ratio $\bar{v}_t$ and Young's modulus $\bar{E}_t$ of the whole pitted region are defined as,

$$\bar{v}_t = \frac{1}{D}\{\frac{E_1'v_1}{3}[(h-d)^3-(h-d-h_1)^3]+\frac{E_2'v_2}{3}[(h_3-d-h_1)^3 -(h_3-d)^3]+\frac{E_3'v_3}{3}[(h_3-d)^3-(-d)^3]\}, \quad (26)$$

$$\bar{E}_t = \frac{12D(1-(\bar{v}_t)^2)}{h^3}, \quad (27)$$

where $E_i'=E_i/(1-v_i^2)$, i denotes the layer number. d signifies the distance between the neutral plane and the bottom surface. D and h are the bending effective stiffness and total thickness of whole plate, respectively.

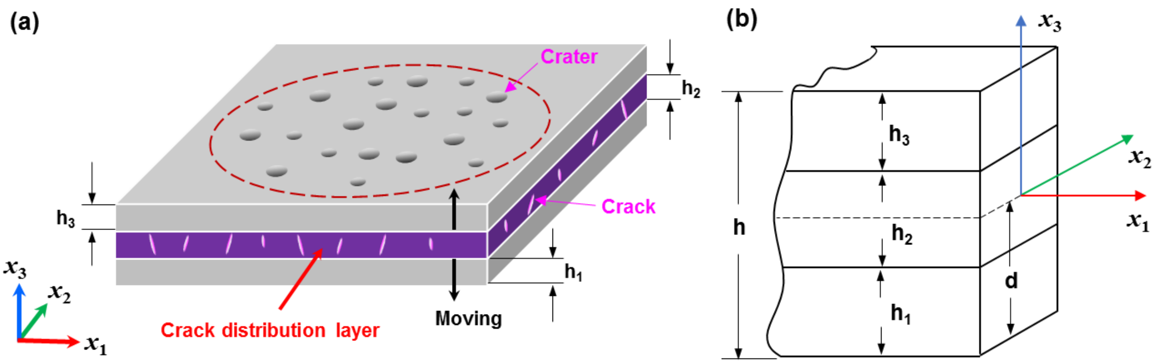

Fig. 5. (a) Schematic of a plate-like structure with micro-cracks distributed in a specific layer; and (b) sketch of a multi-layered model.

Based on the above derivation, a 5 mm-thick plate with micro-cracks uniformly distributed in a 1 mm-thick layer is adopted to analytically examine the effect of crack distribution on the elastic moduli. To be consistent with experimentally observation in our previous work [9], the crack density is set to be 0.01, and other parameters are referred to the Table 1. As demonstrated in Fig. 6, it is worth noting that both the Young's modulus and Poisson's ratio degenerate significantly when micro-cracks distributed in the layer near to the plate surface.

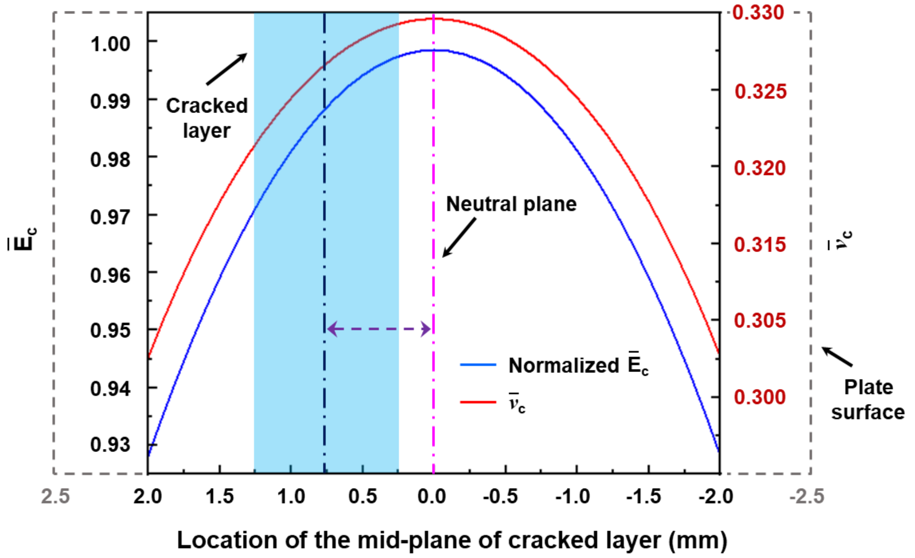

Fig. 6. Effective elastic moduli of a pitted plate with micro-cracks ($\overline{E}_c$ is normalized by its value at pristine state).

To evaluate the ultrasonic nonlinearity induced by the changing of elastic moduli due to the distributed micro-cracks, a nonlinearity parameter is introduced based on a micromechanics model [48], as

$$\begin{aligned}\beta_{cra} &= 1 - \frac{(1+\nu)(1-2\nu)}{(1-\nu)E}\frac{(1-\bar{\nu}_t)\bar{E}_t}{(1+\bar{\nu}_t)(1-2\bar{\nu}_t)} \\ &= 1 - \frac{(1+\nu)(1-2\nu)}{(1-\nu)E}\frac{12D}{h^3}\left(1+\frac{(\bar{\nu}_t)^2}{1-2\bar{\nu}_t}\right),\end{aligned} \quad (28)$$

It is apparent that the degradation of elastic moduli of materials in the pitted region leads to the increasing of ultrasonic nonlinearity, which is positively related to the crack density and distribution.

2.5. Nonlinear Damage Index Definition

The above modeling of ultrasonic nonlinearity generation (*i.e.*, high-order harmonics), due to the interaction of propagating GUWs with various modalities of pitting damage (or nonlinear source), provide a theoretical basis for accurate evaluation of pitting-type damage, serving as the cornerstone of this study. On this basis, a *nonlinear damage index* (*NDI*) is established to quantify the relationship between the ultrasonic nonlinearity and the pitting damage severity, which is defined as

$$NDI = \frac{A^{2\omega}}{(A^{\omega})^2}, \quad (29)$$

where A^{ω} denotes the modal amplitude of measured GUW at ω, and $A^{2\omega}$ the total modal amplitude of measured second harmonics at 2ω, attributing to the IMN, GMN and pitting damage-induced ultrasonic nonlinearities.

3. Proof-of-concept Using Finite Element Method

For a quantitative proof of the theoretical analysis in the preceding Section 2, FE-based methods, including nonlinear Semi-Analytical Finite Element (SAFE) approach and FE models, are performed. Both the intact plate and pitting-damaged plate with various types of damages (*e.g.*, craters, plastic deformation and micro-cracks) in materials are taken into account to gain an insight into the generation and accumulation mechanism of second harmonics behind the interaction of probing GUWs with pitting damage. All possible ultrasonic nonlinearities arising from different types of nonlinear sources in pitted region, *i.e.*, the IMN, GMN, PMN, and CAN, are then investigated to canvass the effect of pitting damage severity on the ultrasonic nonlinearity in GUWs and the mode sensibility for pitting damage evaluation.

3.1. Numerical Modeling of Pitting Damage

2D FE models for both intact and pitting-damaged plates (2 mm thick, 1000 mm long) are developed using the commercial software ABAQUS®/EXPLICIT, respectively, as schematically displayed in Fig. 7. Four-node reduced-integration plane strain elements (CPE4R) are utilized to discretize these FE models. Regarding the intact plate, two types of nonlinear sources, *i.e.*, the IMN and GMN are taken into consideration. For the pitting-damaged plate, a 40 mm-length pitted region (L_{pitted}) is established, which is 80 mm (L_{dis}) to the left boundary of the plate. In addition, ten pitting craters (0.6 mm in diameter) are uniformly distributed at the surface of the pitted region with an interval of 4 mm. Besides the above two nonlinear sources, additional PMN and CAN are introduced to the pitted region.

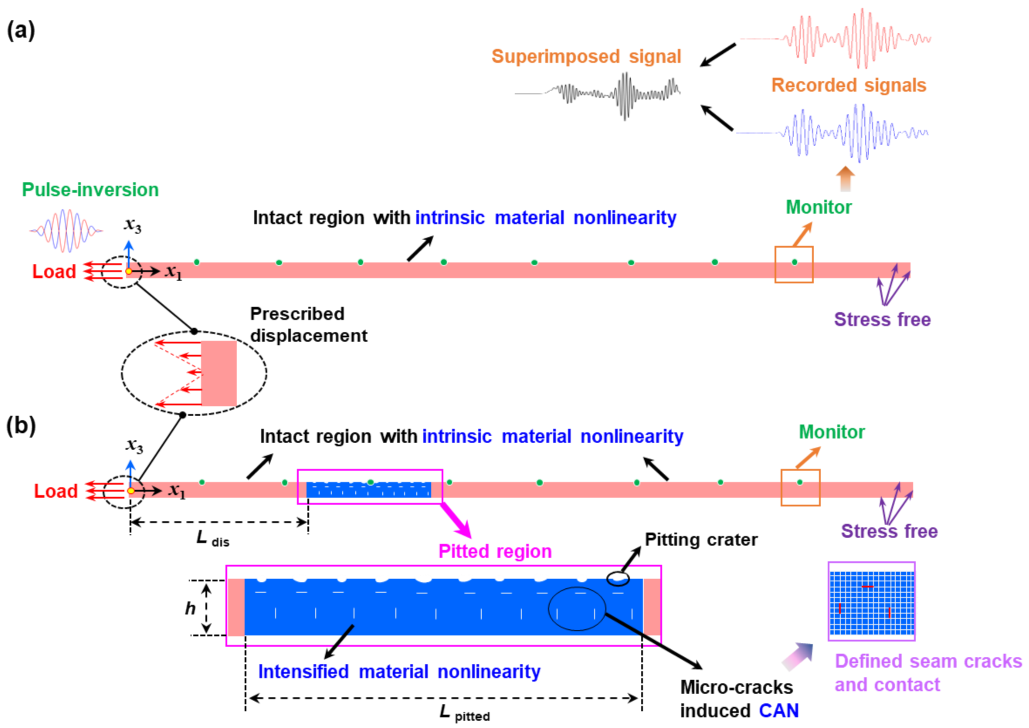

Fig. 7. Schematic of plate-like waveguides for 2D FE models: (a) intact plate; and (b) pitting-damaged plate containing a pitted region.

The numerical modeling of IMN, GMN, and PMN is realized by introducing the modified nonlinear constitutive equations (*i.e.*, Eqs. (2) and (14)) to ABAQUS®/ EXPLICIT via the user defined subroutine VUMAT. The implementation of modeling can be detailed as follows:

(1) To model the linear elastic plate (LEP) without IMN and GMN, both the TOECs and the term of $C_{ijln}\delta_{km} + C_{jnkl}\delta_{im} + C_{jlmn}\delta_{ik}$ in Eq. (2) are zero. Then the Eq. (2) is simplified to the linear Hooke' Law, showing no second harmonic component;

(2) To only model the GMN, the TOECs are set to be zero, and the term of $C_{ijln}\delta_{km} + C_{jnkl}\delta_{im} + C_{jlmn}\delta_{ik}$ is considered;

(3) To model the IMN alone, the TOECs are defined using the parameters in Table 1, and the term of $C_{ijln}\delta_{km} + C_{jnkl}\delta_{im} + C_{jlmn}\delta_{ik}$ equals zero. In reality, both the IMN and GMN must be considered in the simulation implementations simultaneously, together called inherent structure nonlinearity (ISN);

(4) To model the PMN in the pitted region, the TOECs are thought to grow equally up to $\alpha\mathcal{A}$, $\alpha\mathcal{B}$ and $\alpha\mathcal{C}$, where α is assumed to be 1.5 (referred to 1.0 for the intact medium), in line with the huge volume compression of material (35~50%) undergoing HVI, as discussed in our previous work [9].

In addition, to model micro-cracks induced CAN in the pitted region, N ($N = 20$) seam cracks with a length of a_{crack} ($a_{crack} = 0.02$ mm) for each are defined and uniformly distributed in this region S_{pitted} ($S_{pitted} = L_{pitted} \times h$), as seen in Fig. 7(b). In accordance with the experimental observations, ten cracks are parallel to the plate surface underneath the craters, together with other cracks perpendicular to the surface. A contact-pair interaction is imposed on each contacting interface of micro-crack, prohibiting the penetration of nodes into opposite surface, to describe the "breathing" manner when the probing GUWs traverse the crack. Moreover, the crack density is set to be 0.01, obtaining via a dimensionless parameter, *i.e.*, $V_{crack} = Na_{crack}^2 / S_{pitted}$. For the complex and randomly distributed micro-cracks, the primary aim of this proposed 2D modeling is to interpret the comprehensive effect of the severity and distributed layer of cracks on the ultrasonic nonlinearity, respectively, ignoring the influence of individual cracks with different dimensional parameters and orientations.

In the simulation models, two representative mode pairs, viz., S0-s0 and S1-s2 at various excitation frequencies, are respectively exploited. Considering that the symmetric modes are dominant by in-plane displacement (*i.e.*, along x_3 direction), as shown in Fig. 8, prescribed in-plane displacement condition is adopted at the left edge of FE model to excite an appropriate probing GUWs (Fig. 7). Besides, stress-free conditions are applied to another boundaries. In attempts to maximize the generation of pure and interested modes, the excited signal at each specified node is scaled referring to the displacement shape of wave modes, which can be calculated by Eqs. (30) and (31) [49]. The excited signal is formulated as $U = U_0 A_H(t) B_h(x_3)$, where U_0 denotes the displacement amplitude of excitation signal (set to be 1×10^{-4} mm). $A_H(t)$ is a ten-cycle Hanning-windowed sinusoidal tone-burst waveform at various excitation frequencies, representing different degrees of internal resonance conditions. $B_h(x_3)$ is the normalized displacement profile of the excitation signal, which is beneficial for the singular generation of interested GUW mode with other unintended modes suppressed.

$$u_{in} = \frac{i(\kappa^2 - p^2)\sin(0.5ph)}{2q\sin(0.5qh)} \cdot \cos(qx_3)Q_1 - ip \cdot \cos(px_3)Q_1, \tag{30}$$

$$u_{out} = \frac{i(\kappa^2 - p^2)\sin(0.5ph)}{2\kappa\sin(0.5qh)} \cdot \sin(qx_3)Q_1 - i\kappa \cdot \sin(px_3)Q_1, \tag{31}$$

where u_{in} and u_{out} are the in-plane and out-of-plane displacements for the symmetric modes, respectively. Q_1 is a constant that can be determined by the stress-free boundary.

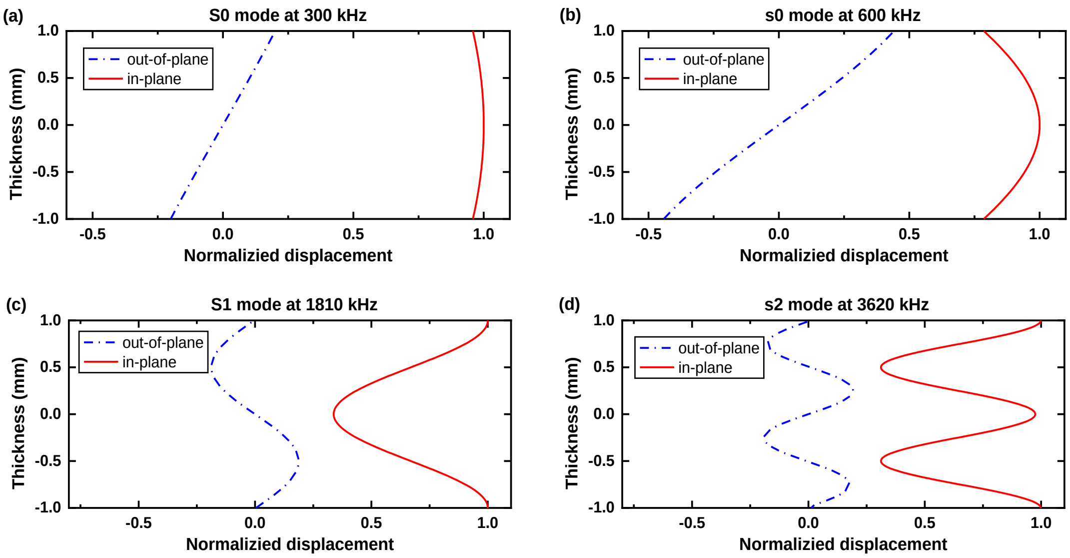

Fig. 8. In-plane and out-of-plane displacement shape of representative symmetric modes for a 2 mm-thick waveguide: (a) S0 mode at 300 kHz; (b) s0 mode at 600 kHz; (c) S1 mode at 1810 kHz; and (d) s2 mode at 3620 kHz.

To warrant simulation accuracy and error convergence, the element size (Δd) should be much smaller than the spatial resolution of $\lambda_L / 24$, where λ_L denotes the wavelength of fundamental wave [28]. Accordingly, for the S0-s0 mode pair, the FE model is discretized with an element sized 0.1 mm only (*i.e.*, 1/30 of the wavelength of s0 mode). Regarding the S1-s2 mode pair, the size of each element is 0.05 mm – 1/50 of the wavelength of s2 mode. To satisfy the stability criteria, time-step (Δt) should be smaller than the time resolution of $\Delta d / c_p^{\omega}$. It is then set to be 2×10^{-9}s, ensuring that the probing GUWs do not travers an element in a step time. Since the representative symmetric modes (*e.g.*, S0, S1, s2 in this work) are dominated by the in-plane displacement along the thickness direction, and the maximum displacement of interested mode appears on the surface (see Fig. 8), GUWs propagating in the plate is continuously observed via acquiring the in-plane displacement on the upper surface at an interval of 20 mm. Notably, the plate in the FE model is 1000 mm length guaranteeing that reflected wave from the right boundary do not interfere with the obtained wave modes of interest.

3.2. Results and Discussions

3.2.1. Mode Excitability and Cumulative Effect for Pitting Damage Evaluation

To facilitate the implementation in practice and enhance the reliability of the developed GUWs-based method, it is required to select an appropriate mode pair which approximately satisfies the internal resonance conditions. In addition, it should manifest a higher excitability than the rest of GUW modes excited simultaneously, guaranteeing that the selected mode pair is preferably excited/sensed. Theoretically, there are an infinite number of mode pairs satisfies the above-mentioned internal resonance (see Fig. 4). Nevertheless, considering the deviation arising from the device and operation, the excitability of high frequency modes, as well as the feasibility of *in-situ* practical application, two representative mode pairs (S1-s2) and (S0-s0) are most widely used for the evaluation of pitting damage.

In general, the selection of optimal GUW modes for damage evaluation is based on the known material properties and phase velocities. However, according to the theoretical derivation in Section 2.5, the HVI induced-pitting damage will cause variations in the elastic moduli of material (or SOECs), *i.e.*, E and ν, which result in the changing of both transverse velocity c_T and longitudinal velocity c_L, as

$$c_T = \sqrt{\frac{\overline{E}_t}{2\rho_0(1+\overline{\nu}_t)}}, \tag{32}$$

$$c_L = \sqrt{\frac{\overline{E}_t(1-\overline{v}_t)}{\rho_0(1+\overline{v}_t)(1-2\overline{v}_t)}}, \tag{33}$$

Accordingly, the degradation of elastic moduli can affect the parameters p and q in the dispersion Eq. (12), which further lead to the variation of dispersion curves in propagating GUWs, as well as the phase-velocity match conditions. For convenience of following analysis, phase velocities of fundamental modes (S0, S1) and secondary modes (s0, s2) for both intact and pitting-damaged plates are calculated via SAFE method using the parameters in Table 1, and separated from the other wave modes, as displayed in Fig. 9. The phase velocities of secondary modes (red and blue lines) are plotted overlapping with that of the fundamental modes, in which point *P* meaning that phase-velocity matching is satisfied. The dashed and solid lines represent the mode pairs for intact and pitting-damaged plates, respectively.

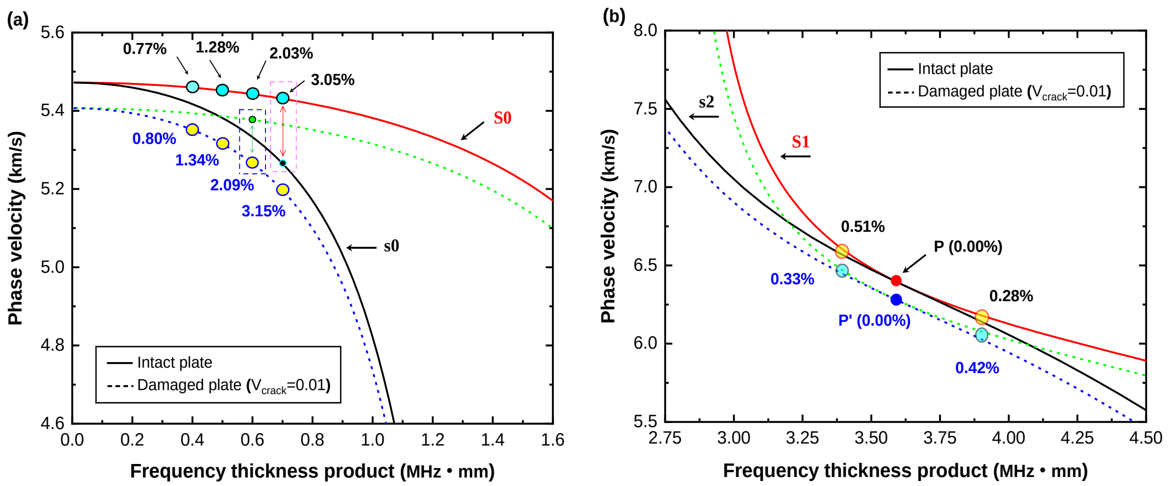

Fig. 9. Phase velocities of selected modes for the intact and pitting-damaged plates: (a) S0-s0 pair; and (b) S1-s2 pair.

It's noteworthy that pitting damage-induced crack leads to the deviation of dispersion curves, and thus the increasing degree of phase-velocity mis-matching condition. This phenomenon provides a basis for selecting preferable mode pairs and frequencies to evaluate pitting damage. The representative points (marked by solid circles) with different excitation frequencies, corresponding to different degrees of phase-velocity mis-matching, are selected for the subsequent numerical analysis.

By way of illustration, numerical results obtained from a 2 mm-thick intact plate at the excitation frequency of 1810 kHz (marked by *P* in Fig. 9) is demonstrated, where the internal resonance conditions are satisfied. It can be observed that the maximum displacement occurs on the surface of the plate when the probing GUW propagates along x_1 direction, as shown in Fig. 10(a), which is in good coincidence with the theoretical results (see Fig. 8). As demonstrated in Figs. 10(b) and (c), only the symmetric GUW modes (S1 and S0) are generated using the prescribed excitation signal, and the wave energy is dominated the fundamental S1 mode. Considering that these measurement points are sufficiently away from the excitation source, S1 mode are fairly isolated from S0 mode in the acquired signals, due to the much greater group velocity of the S1 mode than that of S0 mode at this exciting frequency. This warrants that S1 mode can be purely extracted, guaranteeing the accuracy of the acquired magnitudes of S1-s2 mode pair, making it prior to other mode pairs for microstructural material damage characterization. In addition, the in-plane displacements of both the 0° phase and 180° out-of-phase inversed GUWs are obtained at the monitoring points and processed via a pulse-inversion technique, with which the spectral energy (acquired using the short-time Fourier Transform (STFT)) at fundamental S1 mode is remarkably mitigated, while the weak energy at sub-harmonics and second harmonic s2 mode (*i.e.*, nonlinearity) stand out, as observed in Fig. 10(d). For the intact plate, the generation of second harmonics owns to the ISN.

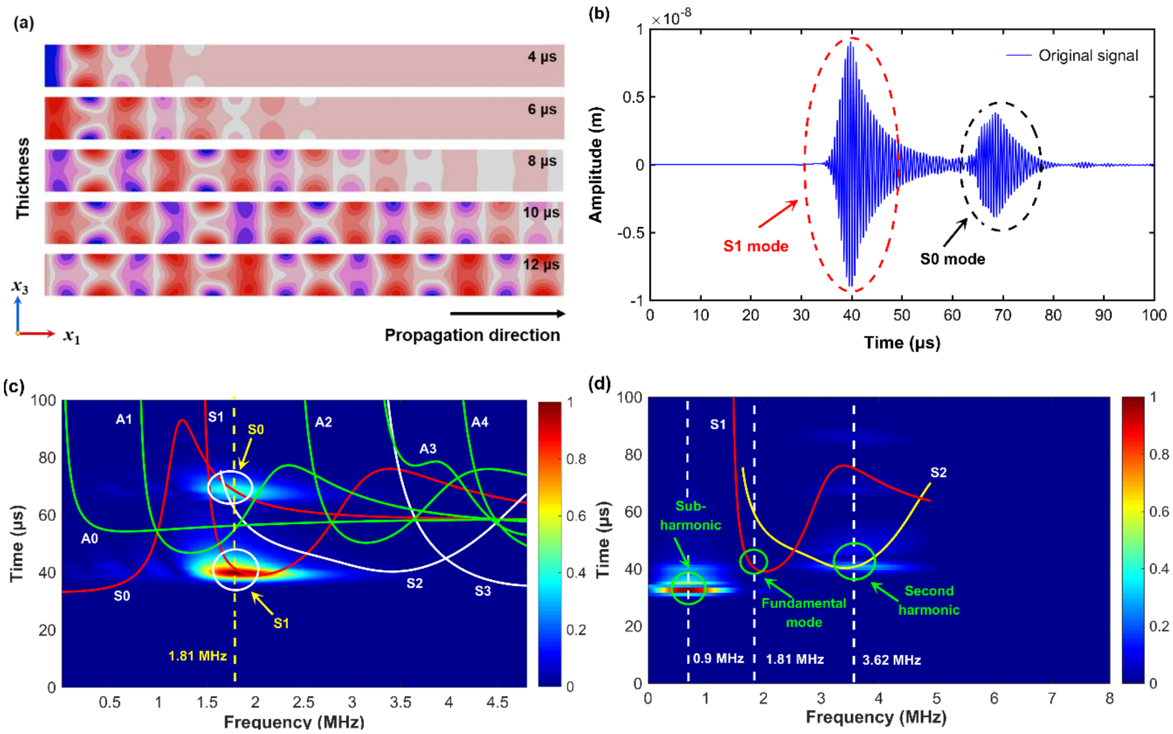

Fig. 10. Signal obtained at the monitoring point 160 mm for a 2 mm-thick intact plate with an excitation frequency 1810 kHz: (a) snapshots of propagating GUWs (in the form of stress contour)[40]; (b) original signal; (c) STFT spectra of the original signal with overlaid group velocity curves; and (d) STFT spectra of the superimposed signals captured via an intact plate with ISN.

Combining the use of SAFE approach and FE models, the cumulative effect of second harmonics against the propagation distance for the interested mode pairs at different excitation frequencies are then investigated, as demonstrated in Fig. 11. For the intact plate, regardless of the excitation frequencies, *NDI* oscillates with respective to the propagating distance in a sinusoidal manner for S0-s0 pair – a phenomenon that can be attributed to the mis-matching in the respective phase and group velocities of two modes (as displayed in Figs. 4 and 9). With the increasing of excitation frequency, the degree of phase-velocity mis-matching is intensified, resulting in the decreasing of oscillation spatial period $(x_1)_n$, as shown in Fig. 11(a). Considering the S1-s2 pair satisfied the phase-velocity matching condition, *NDI* demonstrates a monotonic and linear growth along the propagating distance, as displayed in Fig. 11(b). While *NDI* also oscillates over the propagating distance in a sinusoidal behavior when the phase-velocity is inaccurately matched. The spatial period and normalized oscillation amplitude obtained from the simulations demonstrate a good coincidence with the SAFE analysis, which can be calculated via Eqs. (11) and (13).

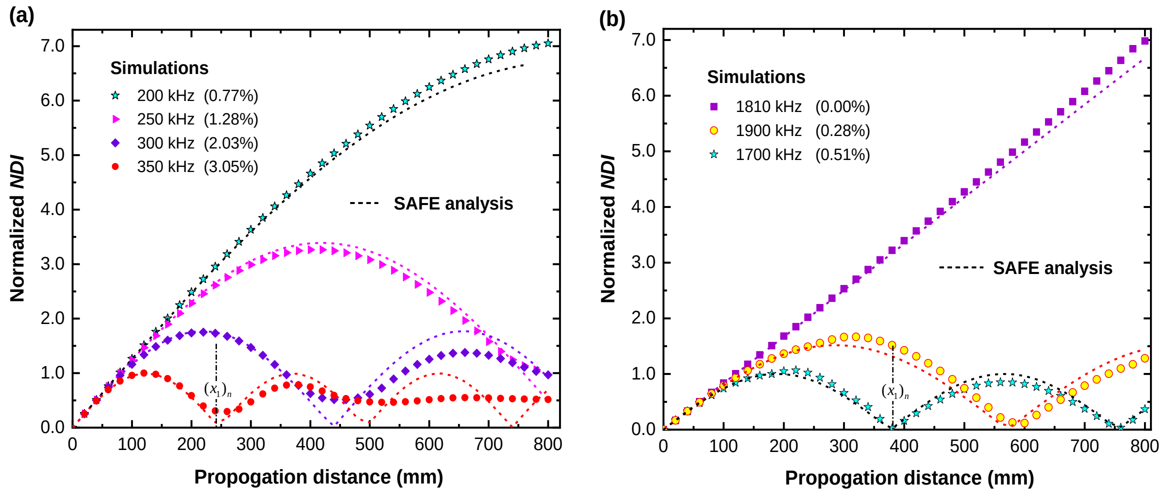

Fig. 11. Comparison of *NDI* obtained via SAFE method and simulations for both intact and damaged plates: (a) S1-s0 mode pair; and (b) S1-s2 mode pair. (Normalized to the value of first peak)

Regarding the pitting-damaged plate, two types of damages are considered separately, *i.e.*, intensified material plasticity, and micro-cracks induced deterioration of elastic moduli of material. To obtain the analytical solution, damages are assumed to uniformly distribute in the whole structure, and effective elastic moduli (calculated by Eq. (25) when $V_{crack} = 0.01$) and enhanced TOECs (the scale factor α is assumed to be 1, 1.5, 2) are introduced to the SAFE approach, respectively. It's noteworthy that accumulation phenomenon of second harmonics in the damaged plate is similar to that of the intact plate. For the pitting damaged plate with cracks only, $(x_1)_n$ decreases with the increasing degree of phase-velocity mis-matching, which is caused by the weakened elastic moduli of material. As displayed in Fig. 12(b), regardless of the intact or damaged plates, $(x_1)_n$ equals when the value of mis-matching degree is approximate. In addition, with micro-cracks induced CAN, the modal amplitude of second harmonic in the probing GUW is intensified, leading to a higher *NDI*. Considering the damaged plate with enhanced material plasticity alone, the enhancement of TOECs contributes to the increase of the power fluxes f_n^{vol} and f_n^{surf}, as illustrated in Eqs. (11) and (29), resulting in the growth of *NDIs*. While $(x_1)_n$ remains unchanged, because the SOECs are assumed to be invariant in the SAFE method, as shown in Fig.12(c). Assuming that plasticity is identical in the whole pitted region, thus the integrated effect of plasticity intensification on the nonlinearity can be quantitatively characterized using the increasing TOECs.

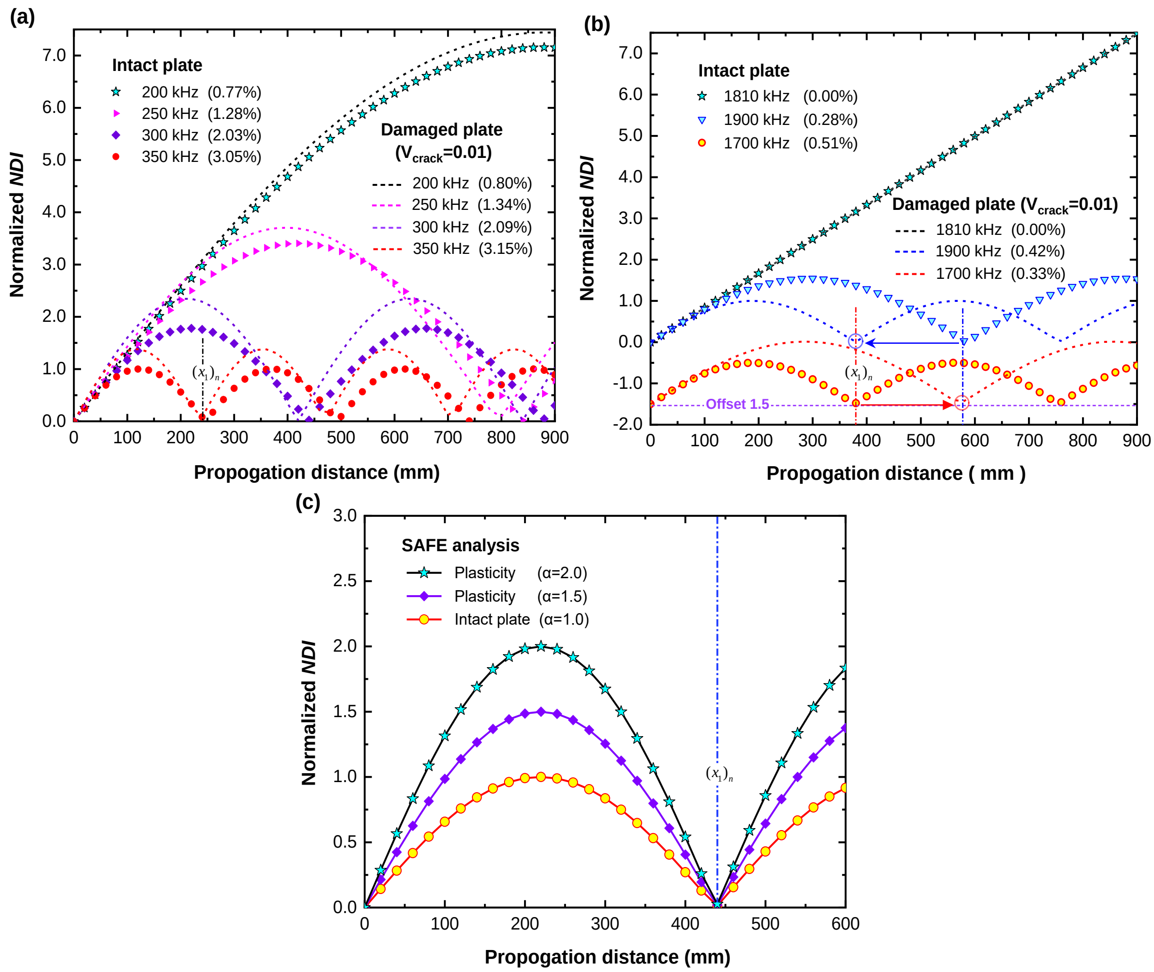

Fig. 12. Comparison of *NDI* obtained by SAFE analysis for both the intact and uniformly damaged plates: (a) S1-s0 pair; (b) S1-s2 pair; and (c) intensification of plasticity at excitation frequency of 300 kHz. (Normalized to the value of first peak).

Based on the above analysis, it can be concluded that *NDI* grows cumulatively along the propagating distance within half of $(x_1)_n$, reaching a peak, because the phase matching condition is approximately satisfied. Then *NDI* gradually decreases to a valley at $(x_1)_n$ as the phase mis-matching dominates. This oscillation trend periodically appears due to the variation of phase mis-matching conditions. The values of $(x_1)_n$ and normalized *NDI* are inversely proportional to the deviation of the phase velocities between the fundamental and second harmonic modes, which is strongly dependent on the excitation frequency. Consequently, to enhance the reliability and improve the sensitivity of the proposed GUW-based method for pitting damage characterization, proper excitation frequencies should be selected, guaranteeing that the weak second harmonics can stand out and continuously accumulate within a certain detection distance.

3.2.2. Generation Mechanism and Sensibility of Second Harmonics

To validate the aforementioned predictions and further analyze the generation mechanism and sensibility of second harmonics, numerical simulations for the pitting-damaged plate are performed, with different excitation frequencies. The numerical results obtained from both the intact plate and damaged plate (2 mm-thick) with a pitted region containing the above different types of nonlinear sources (as discussed in Section 3.1) are compared. Taking the case at the exciting frequency of 300 kHz as an example, the Fast Fourier Transform (FFT) is adopted to extract the magnitudes of both fundamental and second harmonic modes from the in-plane displacement obtained via the intact plate, as shown in Fig. 13. It is obviously that there is indiscernible change in the amplitudes of fundamental modes (*i.e.*, linear feature, A^{ω}) at 300 kHz, indicating its insensitivity to inherent material imperfections, but a conspicuous difference for the second harmonics (*i.e.*, nonlinear feature, $A^{2\omega}$) at 600 kHz. Exemplarily, second harmonic is not observed in the linear elastic pristine plate (black dashed line), while it is generated in the intact plate with IMN and GMN, respectively. It is also interesting to see that the amplitude of the second harmonic generated by the IMN is much greater than that of the GMN, which means that the IMN plays a dominant role in the generating of second harmonics in the intact plate. Together, both of the IMN and GMN, namely ISN, jointly give rise to the accumulation of second harmonics in the plate, which must be considered in the simulation implementations simultaneously.

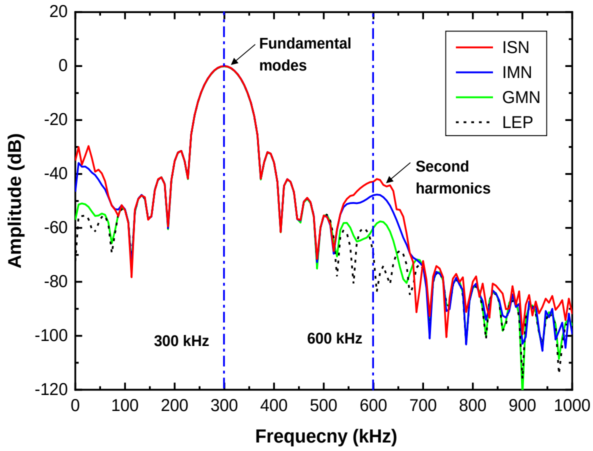

Fig. 13. FFT spectra of signals obtained at the monitoring point 220 mm for an intact plate using the LEP, GMN, and IMN stress-strain constitutive models, respectively.

For the pitting-damaged plate, with the use of a pulse-inversion technique, the spectral energy of fundamental waves (signified by $S_0^{\omega_0}$) is significantly mitigated, while the weak energy of second harmonics (signified by $S_0^{2\omega_0}$) is enhanced (obtained via STFT) , as well as the sub-harmonics ($\omega_0/2$), as displayed in Fig. 14. Note that the second harmonics are generated mainly owing to the ISN for the intact plate. Compared to the intact plate, the spectral energy at $S_0^{2\omega_0}$ obtained from the pitting-damaged plate is increased phenomenally. It is clearly observed that among various types of nonlinear sources, the PMN due to enhanced plasticity is remarkably stronger than that of the ISN, while it is much weaker than that owing to “breathing” cracks-induced CAN. Together, the ISN, PMN and CAN jointly give rise to the generation and cumulation of second harmonics in the plate containing pitting damage, which will be considered in the simulation implementations in the following studies.

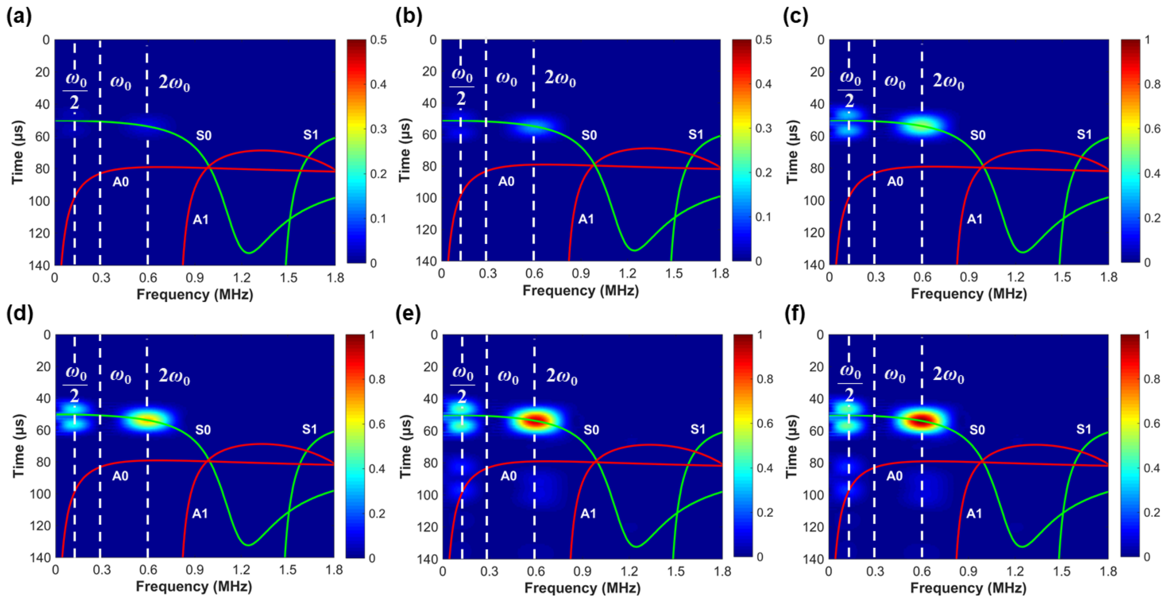

Fig. 14. STFT spectra of superimposed signals obtained at monitoring point 220 mm for a 2 mm-thick plate containing different types of nonlinear sources (excitation frequency is 300 kHz): (a) linear elastic plate; (b) intact plate with GMN; (c) intact plate with ISN; (d) pitted plate with ISN and PMN; (e) pitted plate with ISN and CAN; and (f) pitted plate with ISN, PMN and CAN. (Normalized to the max value of STFT spectra for the Case (f))

To take a step further, *NDIs* are obtained using Eq. (29) along the propagating distance and various types of nonlinear sources for both S0-s0 and S1-s2 mode pairs at different excitation frequencies, as presented in Fig. 15. For an easy comparison, *NDIs* are normalized with respect to the first peak value (marked by the dash line) of the *NDI* acquired from the intact plate in the same case. As observed, *NDI* oscillates against the propagating distance, attributing to the mis-matching of representative phase velocities (see Figs. 15(b)-(f) and (h)); while *NDI* demonstrates a monotonic and linear growth along the propagating distance when the mode pair has the identical or approximate phase velocities, quasi-satisfied the internal resonance conditions (Figs. 15(a) and (g)). Regardless of the excitation frequencies, *NDI* obtained in the pitted plate (with PMN, CAN, or both) grows significantly after traversing the pitted region, due to the interaction between pitting damage and the probing GUWs. This phenomenon is remarkable particularly when the probing GUWs do not satisfy the internal resonance conditions, as displayed in Figs. 15(b)-(f) and (h).

It is noteworthy that with the increasing degree of phase-velocity mis-matching, the oscillation spatial period $(x_1)_n$ significantly decreases (Figs. 15(a)-(d), and Figs.15(g)-(h)), while the pitting damage-induced nonlinearity stands out with comparable effectiveness, in particular the crack-induced CAN, as marked by pink arrows. These features are beneficial for the discerning and extraction of pitting damage-induced nonlinearity. Therefore, it is not of necessity to meet the prerequisite of internal resonance conditions. Generally, compared to the intact plate, both the peak and valley for an uniformly damaged plate will appear in advance due to the increasing degree of phase-velocity mis-matching, as shown in Fig. 12. However, this phenomenon is changed for a localized pitting-damaged plate owing to the modulation of pitted region on the propagating GUWs. As revealed in Fig. 15(b)-(d) and (h):

(1) *NDI* obtained from the pitting-damage plate reaches the peak earlier than that of the intact plate with the excitation frequencies 250 kHz and 1900 kHz, because that $(x_1)_n$ is large enough and the pitted region is far away from the peak, thus the sharply intensified *NDI* after traversing the pitted region will have enough distance to recover its regular propagation pattern in an uniformly plate;

(2) *NDI* reaches the peak equal to that of the intact plate with the exciting frequency 300 kHz, which can be attributed to the decreasing of $(x_1)_n$, leading to no enough distance to recover its regular propagation pattern after a dramatic intensification, and subsequently a slight delayed arrival of the peak. While, it arrives the valley in advance owing to the recovery of propagation GUWs;

(3) with the further or remarkable decreasing of $(x_1)_n$, as seen in Fig.15(d), the pitting damage-induced significantly enhancement of *NDI* delays the appearance of both the peak and valley.

The above findings are proven again in Figs. 15(d)-(f), when the pitted region is located on both the rising and trailing edges of the oscillation period, respectively, with different distance to the exciting source (L_{pitted}). Compared to the pitted region on the rising edge, more remarkable discrepancy can be observed between the ISN- and CAN-induced *NDIs* for that on the trailing edge, which is beneficial to stand out the crack-induced ultrasonic nonlinearity.

Accordingly, the mode pair at a relatively higher degree of phase-velocity mis-matching is more feasible and sensitive to characterize the pitting damage. While, in order to obtain a sufficiently large and discernible *NDI*, the pitted region is better located within the first oscillation period, because *NDI* attenuates with the increasing of propagation distance or oscillation period. Limited to the size of pitted region (typically 40~100 mm) and the value of $(x_1)_n$, the maximum detection distance between the actuator and sensor should better shorter than half of $(x_1)_n$, guaranteeing that the weak second harmonics can stand out and continuously accumulate within an enough propagation distance.

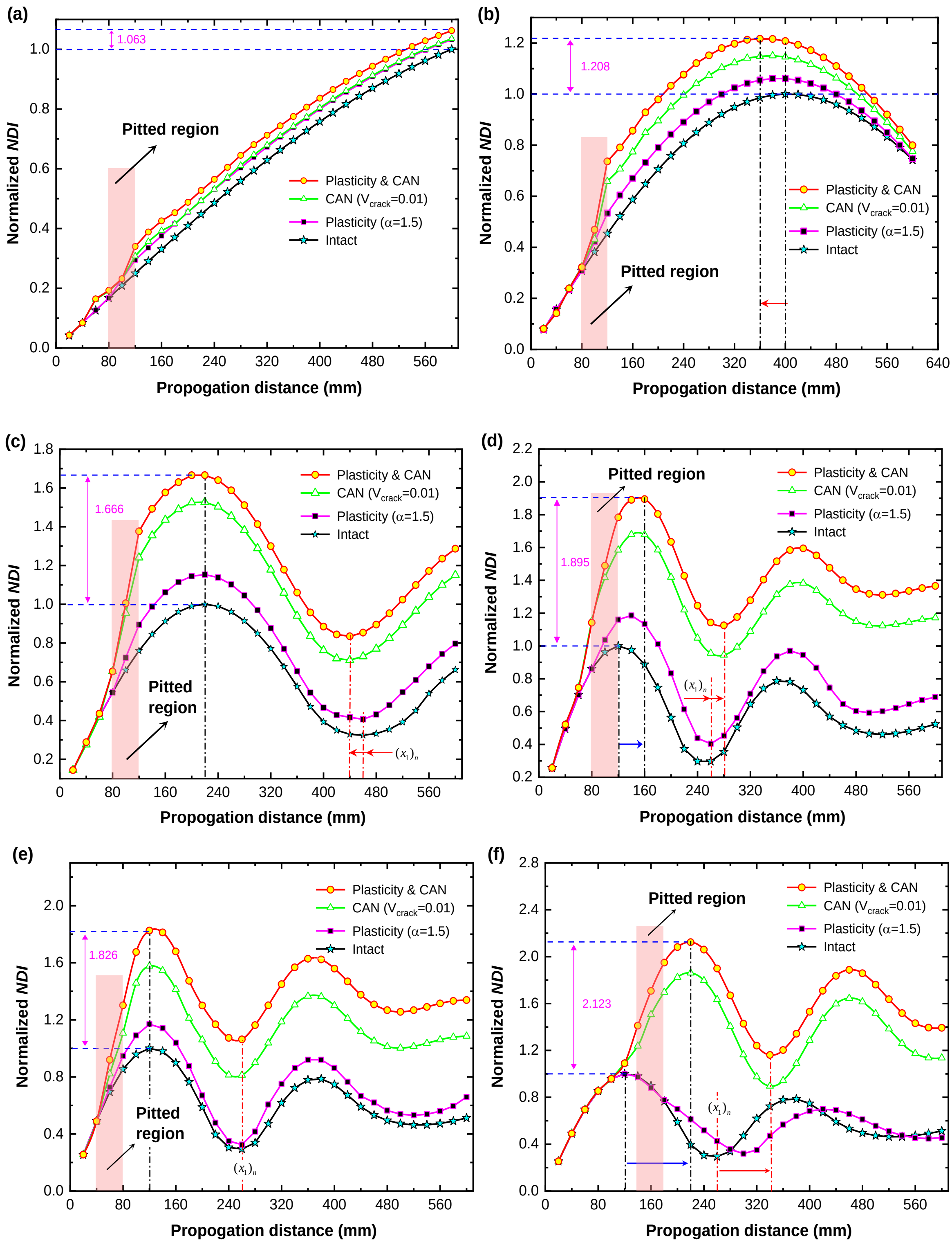
(a)
(b)
(c)
(d)
(e)
(f)
Normalized NDI
Propogation distance (mm)
Pitted region
Plasticity & CAN
CAN (V_crack=0.01)
Plasticity (α=1.5)
Intact
1.063
1.208
1.666
1.895
1.826
2.123
$(x_1)_n$

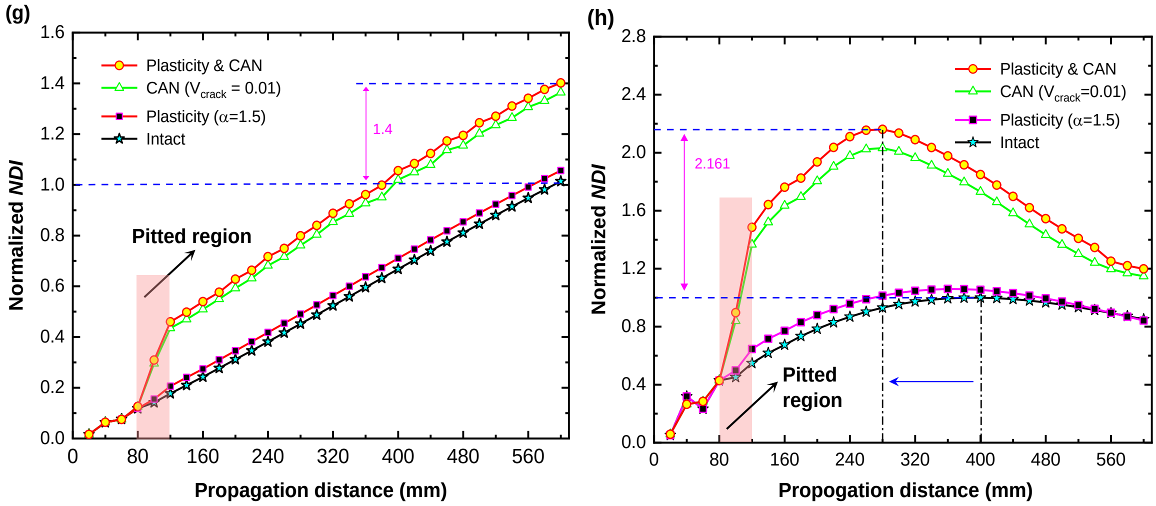

Fig. 15. Normalized *NDIs* obtained in simulations using mode pairs S0-s0 and S1-s2 with different excitation frequencies: (a) 200 kHz; (b) 250 kHz; (c) 300 kHz; (d) 350 kHz; (e) 350 kHz; (f) 350 kHz; (g) 1810 kHz; and (h) 1900 kHz.

3.2.3. Effect of Pitting Damage Severity and Distribution on Nonlinearity

Note that pitting damage can be different under the variation of impact conditions, targeting at giving an insight into the effect of pitting damage severity (*e.g.*, pitted region size and crack density) and distribution on ultrasonic nonlinearity, a series of 2D FE models are performed, as detailed in Table 2. ISN, PMN ($\alpha = 1.5$) and CAN are considered in the pitted region, the modeling procedures remain the same as those described in Section 3.1.

Table 2. 2D FE models used for investigating the effect of pitting damage severity and distribution.

Case	h (mm)	L_{pitted} (mm)	N	a_{crack} (mm)	V_{crack}	Crack distribution	Mode pair	Excitation frequency
1	2	20	10	0. 2	0.01	Uniformly distributed	S0-s0 600~1200 kHz mm	300 kHz
2		30	15		0.01			
3		40	20		0.01			
4		40	25		0.0125			
5		40	30		0.015			
6	5	40	50		0.01	Surface	S1-s2	720 /760 kHz
7		40	50		0.01	Sub-surface	3.60~7.20 MHz mm	
8		40	50		0.01	Mid-plane	3.80~7.60 MHz mm	

As illuminated in Fig. 16, a conspicuous increase in *NDI* is easily noticed with the increasing of pitted region length, as well as the crack density, indicating that the proposed *NDI* is sensitive to the occurrence of pitting damage, which can be adopted to precisely evaluate the severity of pitting damage. It is worth noting that the oscillation spatial period $(x_1)_n$ slightly decreases for the plate with pitted region, attributing to the changing of phase-velocity mis-matching condition, which is caused by the weakened elastic moduli of material. The simulation results are in accordance with the foregoing analytical solutions.

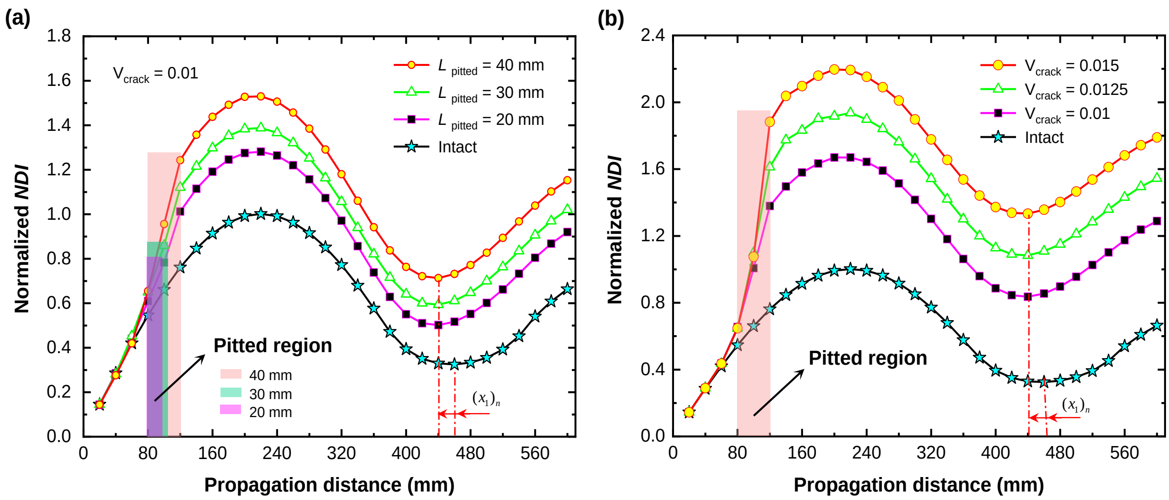

Fig. 16. *NDI* obtained in simulations using mode pair S0-s0 with excitation frequency of 300 kHz: (a) *NDI vs*. the pitted region length; and (b) *NDI vs*. the crack density. (Normalized to the value of first peak).

In addition, to facilitate the investigation of crack distribution induced discrepancy in ultrasonic nonlinearity, a 5 mm-thick 2D FE model is developed with cracks uniformly distributed in different layer (*i.e.*, surface, sub-surface and mid-plane layers with a thickness of 2 mm) in the pitted region, as schematically depicted in Fig. 17(a). The central frequencies of 720 kHz and 760 kHz are applied to generate the S1-s2 mode pair, satisfying the phase-velocity matching and mis-matching conditions, respectively. Regardless of the internal resonance conditions, *NDI* for the pitting-damaged plate increases drastically after traversing the pitted region when compared to that of the intact plate, as illustrated in Figs. 17(b) and (c). When the layer containing micro-cracks moves from the mid-plane to the surface of the plate, a conspicuous increase of the *NDI* is easily noticed, in particular the mode pair with phase-velocity mis-matching. This is because, as theoretically analyzed in Section 2.4, in the pitted region, both the Young's modulus and Poisson's ratio degenerate significantly when the micro-cracks distributed in the layer near to the plate surface, leading to the intensification of ultrasonic nonlinearity.

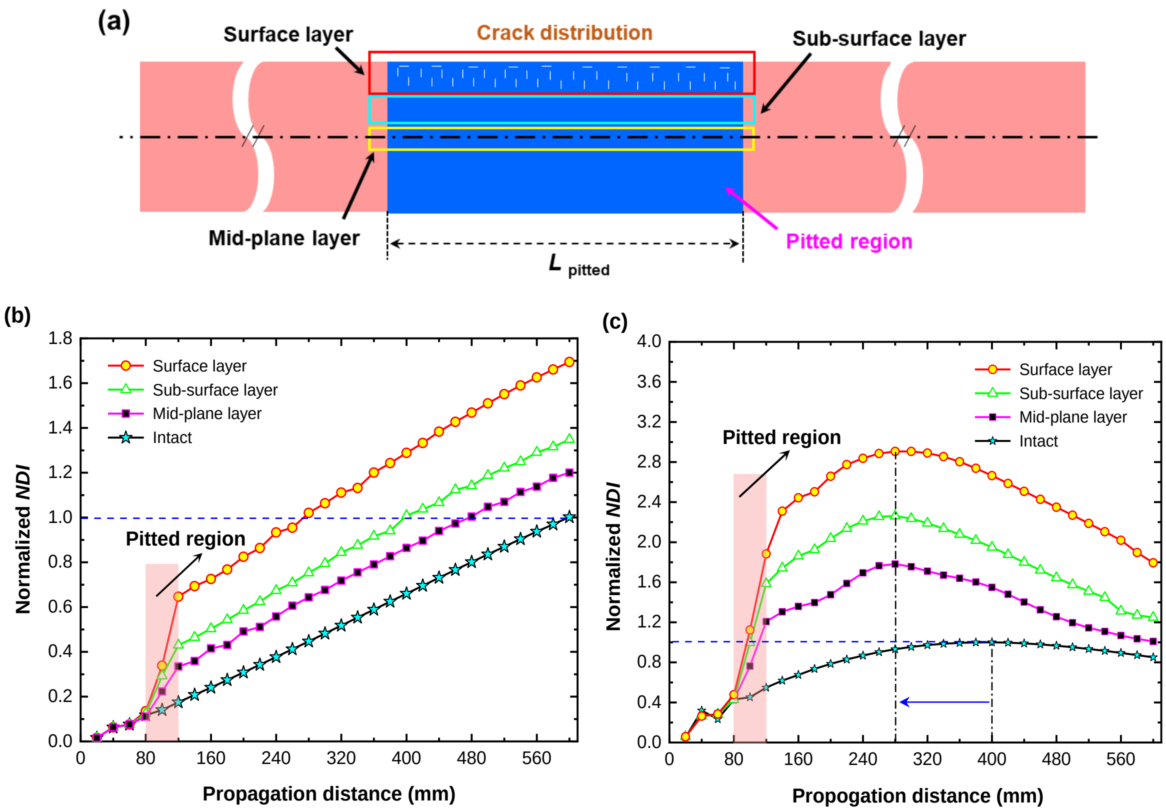

Fig. 17. (a) Schematic of FE model with cracks distributed in different layer of the pitted region; (b) and (c) *NDI* obtained in simulations via S1-s2 mode pair with excitation frequency 720 kHz and 760 kHz, respectively. (Normalized to the value of first peak).

The SAFE and simulation results have accentuated the significant influence of the pitting damage (including three types of damage sources) on the generation and accumulation of nonlinearity in GUWs, and inversely the abnormal growth of nonlinearity in probing GUWs can be applied to quantitively evaluate the pitting damage severity, as illustrated by the experimental application in the following Section. Simultaneously, these findings also provide a basis for the selection of preferable extraction frequency and detection distance for damage evaluation. While the proposed 2D models cannot be used to scrutinize the crack orientation induced wave-scattering.

4. Experimental Application: Characterizing HVI-induced Pitting Damage

The theoretical and numerical modelling aspires to a new structural health monitoring framework for guiding the experiment design of pitting-type damage evaluation in space assets, including the proper sensor network (or detection distance) design, appropriate mode pair and preferable frequency selection, *etc*. Most importantly, to break through a bottleneck of GUW-based detection when extended to quantitative evaluation of multitudinous damage disorderedly scattered within a single inspection region. These proposed modeling techniques are experimentally validated using an interested S0-s0 mode pair with different degree of phase-velocity mis-matching conditions, in which highly complex pitting damage in the rear wall layer of an AL-Whipple shield, endangered by HVI, is quantitatively characterized.

4.1. Experiment Set-up

To facilitate the experimental validation, HVI test is performed using a two-stage light gas gun to generate pitting damage in a plate-like structure. In the experiment, a spherical projectile (AL-2017, Ø 3.2 mm) is accelerated to 4.13 km/s to impact a typical dual-layered Whipple shield, consisting of a 1 mm-thick bumper layer (2024-T4) and a rear wall layer (5A06, 3 mm × 500 mm × 500 mm in dimension) with a shield spacing of 100 mm, as schematically displayed in Fig. 18(a). The bumper layer is penetrated by the projectile owing to the vast kinetic energy, and the shattered projectile, together with some portions of jetted material of the bumper layer form a debris cloud, which subsequently impacts the rear wall. Consequently, pitting damage, featuring multitudinous small-scale craters and cracks, are induced and disorderedly clustered over a large region, as photographed in Fig. 18(b). The severity of pitting damage in the three typical regions (*i.e.*, D_{cc}, D_{rc} and D_{99}) are usually different obviously.

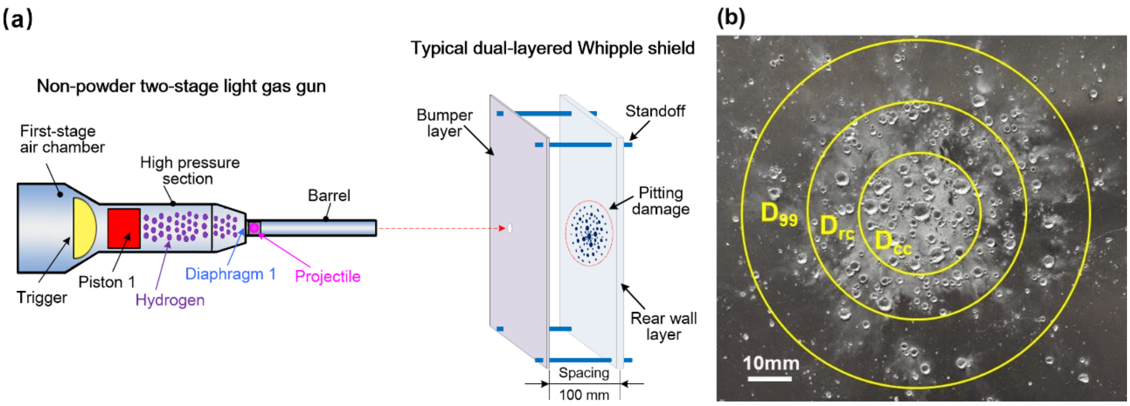

Fig. 18. (a) Schematic of HVI test set-up; and (b) photography of HVI-induced pitting damage.

Upon the HVI experiment, pitting damage in the rear wall is detected and characterized using proposed nonlinear ultrasonic evaluation approach. Fig. 19 demonstrates the schematic of GUWs-based experimental set-up. In the experiments, an *in-situ* square sensing network, consisting of 40 miniaturized, lightweight lead zirconate titanate (PZT) wafers (PSN33, Φ5 mm, thickness: 0.48 mm), is developed, rendering up to 22 scanning paths, with several paths traversing the pitted region, as displayed in Fig. 19. The scanning path is 160 mm in length with an interval of 16 mm to each other, covering an inspection area of 160 mm × 160 mm. The RITEC advanced ultrasonic system (RITEC® RAM-5000 SNAP) is used to generate a ten-cycle Hanning-windowed sinusoidal tone-burst signal, which is then input to the low-pass filter to filter out the undesired nonlinearities related to the system before being fed to the PZT. The mode pair S0-s0 with various excitation frequencies as investigated in preceding Sections are excited using this system. To suppress the measurement uncertainty, the response GUW signals are recorded by an oscilloscope (Agilent DSO 9064A) with an average of 256 times. The procedure of signal processing for the experiments remains the same with that of the FE simulations.

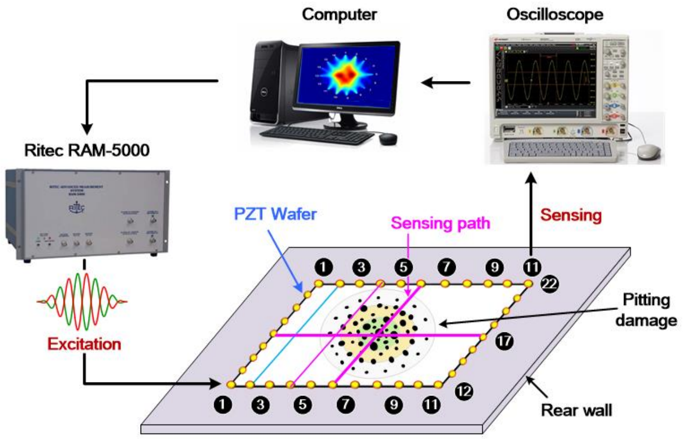

Fig. 19. Schematic illustration of GUWs-based experimental set-up for pitting damage evaluation.

4.2. Results and Discussions

As discussed in the preceding Sections, the mode pairs that satisfied the approximate phase-velocity matching conditions in a range of frequency are more effective to evaluate the pitting damage, attributing to their less dispersive property in phase velocities. Considering that the mode pair with high frequency (higher than 1.0 MHz) are usually weak and difficult to generated via PZT-based sensor network for *in-situ* or on-line monitoring, low frequency mode pair (S0-s0) with quasi phase-velocity matching are mostly used. Accordingly, four investigated frequencies above, *i.e.*, 200 kHz, 250 kHz, 300 kHz, and 350 kHz, are used here to analyze the nonlinear features of GUWs in pitting-damaged rear wall, and validate the numerical modeling.

Obviously, the severities of pitting damage in the three typical regions, *i.e.*, D_{cc}, D_{rc} and D_{99} have significant discrepancy, resulting in distinct amounts of energy transferred from the fundamental mode to the second harmonics against different scanning paths. Taking three representative scanning paths (*i.e.*, Path 1, Path 5 and Path 6) containing different severity of pitting damage at the excited frequency 300 kHz as examples, as interpreted in Fig. 20(a), and the generation of second harmonics $S_0^{2\omega_0}$ via these paths are scrutinized. The spectra energy of the original GUWs and the extracted secondary GUWs for the two representative scanning paths (Path 1 and Path 6), when it respectively traverses the intact region and pitted region center, are obtained via STFT and a pulse-inversion technique, as shown in Figs. 20(c) and (d), respectively.

It is worth noting that the probing $S_0^{\omega_0}$ mode arrives at the monitoring point first due to the much greater group velocity, guaranteeing that it can be fairly separated from other GUW modes in the acquired signals. Such a trait is beneficial for the pure extraction of the fundamental modes and second harmonics. Note that the incident energy of probing GUWs transfers from the fundamental mode to the second harmonics (Fig.20(d)) for the Path 6 containing damage, from which the amplitudes of $S_0^{\omega_0}$ and $S_0^{2\omega_0}$ modes are obtained, as displayed in Figs. 20(e) and (f), on which basis *NDI* can be ascertained via Eq. (29) for each scanning path. It can be observed that HVI-induced damages in the rear wall interrogated in this paper are small-scale, and thus the effect of wave scattering and mode conversion caused by this type of damages on the proposed *NDI* is negligible. It is also noteworthy that the amplitude of $S_0^{2\omega_0}$ mode grows with the enhancement of pitting damage, resulting in a higher *NDI*, which demonstrates a good consistency with the theoretical and numerical analyses. Inversely, it is feasible to quantitatively evaluate the severity of pitting damage in all scanning paths using the defined *NDI*s, as shown in Fig. 21. All these *NDI*s adopted in the experimental application are calculated in the current status, without entailing a benchmark process against any baseline signals from the intact plate under certain conditions, offering a baseline-free mechanism for pitting damage characterization.

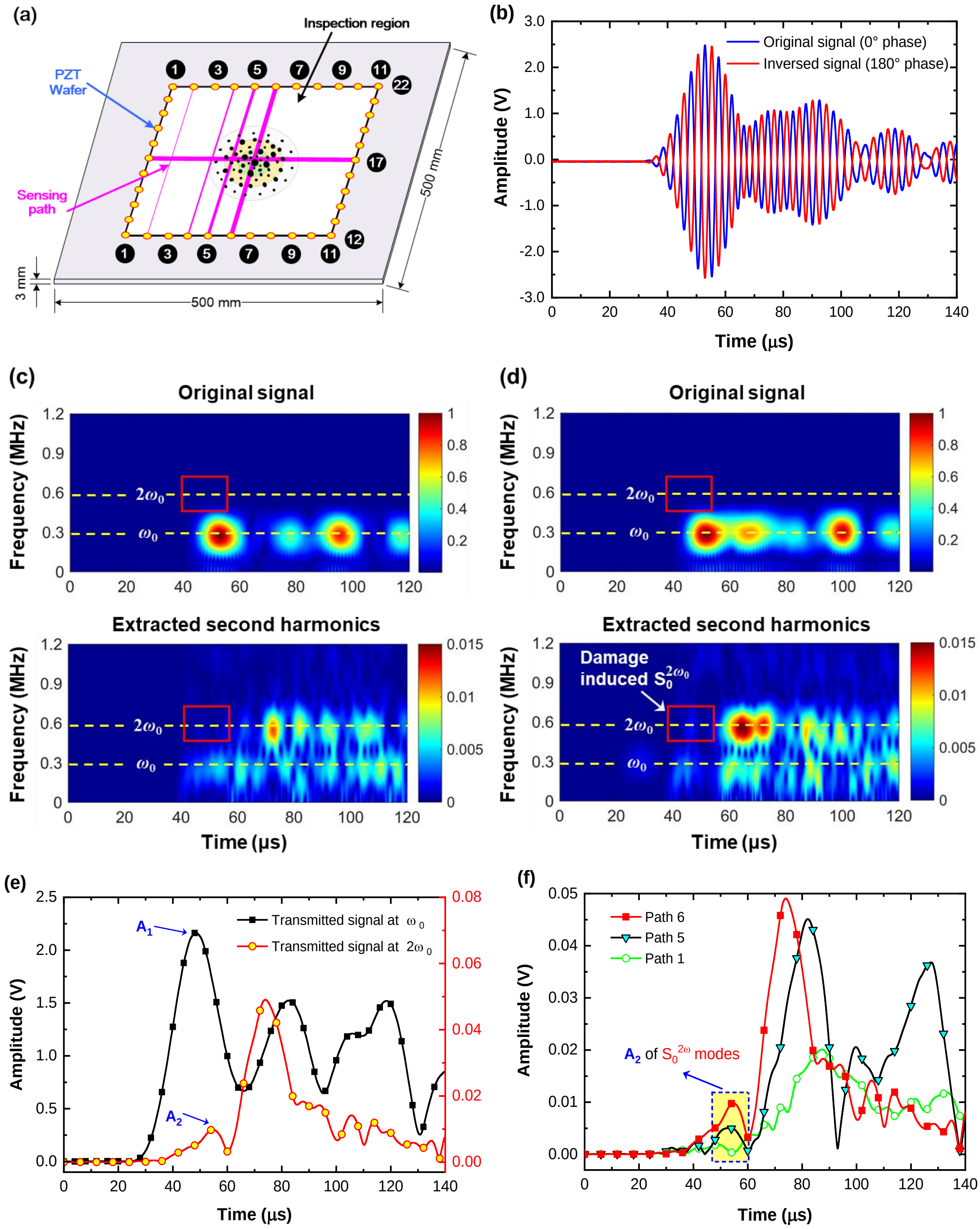

Fig. 20. (a) Sketch of the *in-situ* PZT-based network for pitting damage evaluation; (b) original signal obtained from scanning Path 6; (c) and (d) STFT spectra of signals obtained via Path 1 and Path 6,

respectively; (e) amplitudes of $S_0^{\omega_0}$ and $S_0^{2\omega_0}$ modes for Path 6; and (f) amplitudes of $S_0^{2\omega_0}$ mode for three typical scanning paths.

To further analyze the sensitivity of S0-s0 pair for characterization of pitting damage, *NDIs* obtained at different excitation frequencies (*i.e.*, 200 kHz, 250 kHz, 300 kHz and 350 kHz) are acquired and compared, as presented in Fig. 21. The *NDI* is normalized with respect to the value that obtained in the intact path, which grows with the increasing intensification of pitting damage. In addition, with the increasing degree of phase-velocity mis-matching (represented by the excitation frequency), *NDI* gradually grows, demonstrating a good consistency with the preceding theoretical and numerical analyses. Consequently, a higher excitation frequency is preferred for low frequency S0-s0 pair to quantitatively characterize the pitting damage.

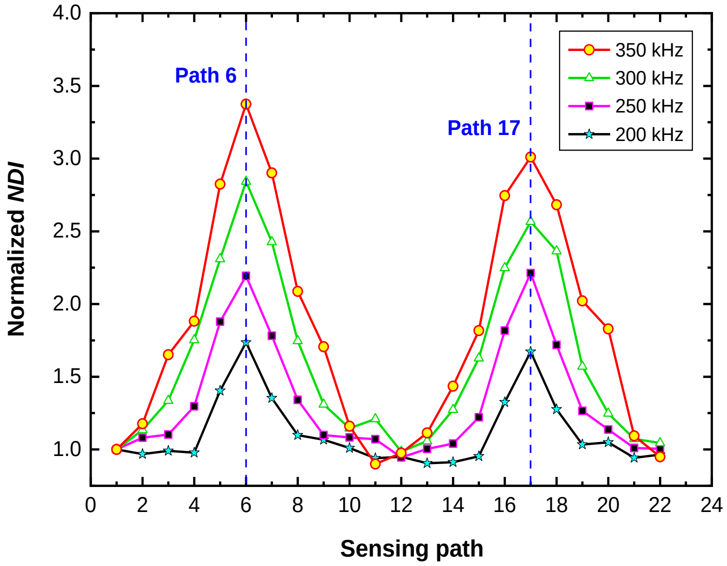

Fig. 21. *NDI* obtained via all sensing paths for the mode pair S0-s0 with different excitation frequencies. (Normalized to the value obtained via sensing path one)

5. Concluding Remarks

Featuring multitudinous localized craters, cracks and diversity of microstructural damages disorderedly clustered over a wide area, pitting damage will cause highly complex wave scattering in the linear features of GUWs. Targeting at quantitatively characterizing HVI-induced pitting damage using nonlinear features (*i.e.*, second harmonics) of the probing GUWs, dedicated theoretical and numerical modeling techniques are performed to interpret the generation mechanism of nonlinearities attributed to the intrinsic material imperfections, as well as HVI-induced enhanced plasticity and micro-cracks. Results from the theoretical analysis, simulations and experiments demonstrate good consistency, revealing that:

(1) the proposed modeling approach is feasible and effective to faithfully simulate and precisely evaluate pitting damage-incurred nonlinearities manifested in ultrasonic waves;

(2) all the mentioned nonlinear sources, including IMN, GMN, PMN and CAN, jointly contribute to the enhancement of nonlinear features in probing GUWs, of which HVI-induced PMN and CAN dominants the generation of second harmonics, in particular the "breathing" cracks-induced CAN;

(3) the ultrasonic nonlinearity, defined as *NDI*, is sensitive to the variation of pitting damage, including the length of pitted region, crack density and distribution;

(4) the detection sensibility and cumulative generation of second harmonics are related to the degree of phase-velocity mis-matching, representing by the excitation frequency. When *NDIs* continuously accumulate within a certain detection distance larger than the size of pitted region, as well as shorter than half of oscillation spatial period, the mode pair at a relatively higher degree of phase-velocity mis-matching is preferred and sensitive to characterize pitting damage.

Essentially, the defined *NDIs* are obtained in the current status, without entailing a benchmark process against baseline signals from an intact counterpart, and thus this proposed method offers a baseline-free mechanism. This study yields a GUW-based SHM scheme for *in-situ* accurately characterizing pitting damage at an embryo stage and surveilling material deterioration progress continuously.

Declaration of Competing Interest

The authors declare that they do not have any financial or nonfinancial conflict of interests

CRediT authorship contribution statement

Wuxiong Cao: Conceptualization, Methodology, Writing-original draft. **Lei Xu:** Methodology, Investigation, Writing-review & editing. **Baojun Pang:** Methodology, Supervision. **Runqiang Chi:** Supervision, Writing-review & editing. **Zhongqing Su:** Methodology, Supervision. **Lei Wang:** Investigation, Validation. **Xiaoyu Wang:** Investigation, Validation, Funding acquisition.

Acknowledgement

This project was funded by the 4th Advance Research Program of Manned Space Flight.

References

[1] Chatterton S, Pennacchi P and Vania A. Electrical pitting of tilting-pad thrust bearings: Modelling and experimental evidence. *Tribol Int* 2016; 103: 475-486.

[2] Raadnui S and Kleesuwan S. Electrical pitting wear debris analysis of grease-lubricated rolling element bearings. *Wear* 2011; 271: 1707-1718.

[3] Qiu Z, Wang S, Zeng Z, et al. Automatic visual defects inspection of wind turbine blades via YOLO-based small object detection approach. *J. Electron. Imaging* 2019; 28(4), 043023.

[4] Jakubowski M. Influence of pitting corrosion on fatigue and corrosion fatigue of ship and offshore structures, part II: load-PIT-crack interaction. *Pol Marit Res* 2015; 22: 57-66.

[5] Metallurgical Consulting. http://www.metalconsult.com/stress-corrosion-cracking-reactor-vessel.html (accessed 20 December 2020).

[6] Mansoori H, Mirzaee R, Esmaeilzadeh F, et al. Pitting corrosion failure analysis of a wet gas

pipeline. *Eng Fail Anal* 2017; 82: 16-25.

[7] Cao W, Wang K, Zhou P, et al. Nonlinear ultrasonic evaluation of disorderedly clustered pitting damage using an in situ sensor network. *Struct Health Monit* 2020; 19(6):1989-2006.

[8] Zhang P, Xu K, Li M, et al. Study of the shielding performance of a Whipple shield enhanced by Ti-Alnylon impedance-graded materials. *Int J Impact Eng* 2019; 124: 23-30.

[9] Cao W, Wang Y, Zhou P, et al. Microstructural material characterization of hypervelocity-impact-induced Pitting Damage. *Int J Mech Sci* 2019; 163:105097.

[10] Madaras E I, Winfree W P, Prosser W H, et al. Nondestructive Evaluation for the Space Shuttle's Wing LeadingEdge. *41st AIAA/ASME/SAE/ASEE Joint Propulsion Conference & Exhibit*, Tucson, Arizona, 10-13 July 2005; AIAA 2005-3630.

[11] Moser D, Poelchau M H, Stark F, et al. Application of nondestructive testing methods to study the damage zone underneath impact craters of MEMIN laboratory experiments. *Meteorit Planet Sci* 2013; 48: 87-98.

[12] Raith M and Grosse C U. In ultrasound tomography on hypervelocity impact targets. In: *19th World Conference on Non-Destructive Testing*, Munich, 13-17 June 2016, p. A4. Berlin: Deutsche Gesellschaft für Zerstörungsfreie Prüfung DGZfP.

[13] Wan T, Wakui T, Naoe T, et al. Pitting damage imaging by non-linear ultrasonic technique: comparison between resonance and non-resonance modes. *Int J Mater Prod Tec* 2013; 46(2-3):141-154.

[14] Bao Q, Yuan S, Guo F, et al. Transmitter beamforming and weighted image fusion-based multiple signal classification algorithm for corrosion monitoring. *Struct Health Monit* 2019; 18(2):621-634.

[15] Ciampa F, Scarselli G, Pickering S, et al. Nonlinear elastic wave tomography for the imaging of corrosion damage. *Ultrasonics* 2015; 62:147-155.

[16] Rao J, Ratassepp M, Lisevych D, et al. On-line corrosion monitoring of plate structures based on guided wave tomography using piezoelectric sensors. *Sensors* 2017; 17(12): 2882.

[17] Zhou C, Su Z, Cheng L. Quantitative evaluation of orientation-specific damage using elastic waves and probability-based diagnostic imaging, *Mech Syst Sign Process* 2011; 25 (6): 2135-2156.

[18] Jhang K-Y. Nonlinear ultrasonic techniques for nondestructive assessment of micro damage in material: a review. *Int J Precis Eng Manuf* 2009; 10: 123-135.

[19] Dutta D, Sohn H, Harries K A, et al. A nonlinear acoustic technique for crack detection in

metallic structures. *Struct Health Monit* 2009; 8(3): 251-262.

[20] Solodov I, Wackerl J, Pfleiderer K, et al. Nonlinear self-modulation and subharmonic acoustic spectroscopyfor damage detection and location. *Appl Phys Lett* 2004; 84: 5386-5388.

[21] Ulrich T, Johnson P A and Müller M, et al. Application of nonlinear dynamics to monitoring progressive fatigue damage in human cortical bone. *Appl Phys Lett* 2007; 91: 213901.

[22] Wang X, Wang X, Hu X, et al. Damage assessment in structural steel subjected to tensile load using nonlinear and linear ultrasonic techniques. *Appl Acoust* 2019; 144: 40-50.

[23] Setyawan W, Henager Jr C H and Hu S. Nonlinear ultrasonic response of voids and Cu precipitates in body-centered cubic Fe. *J Appl Phys* 2018; 124(3): 035104.

[24] Shui G, Wang Y, Huang P, et al. Nonlinear ultrasonic evaluation of the fatigue damage of adhesive joints. *NDT&E Int* 2015; 70: 9-15.

[25] Wang K, Liu M, Cao W, et al. Detection and sizing of disbond in multilayer bonded structure using modally selective guided wave. *Struct Health Monit* 2021; 20(3): 904-916

[26] Chillara V K and Lissenden C J. Nonlinear guided waves in plates undergoing localized microstructural changes. *AIP Conf Proc* 2015; 1650 (1): 1561-1569.

[27] Cantrell J H. Substructural organization, dislocation plasticity and harmonic generation in cyclically stressed wavy slip metals. *Proc Royal Soc London, Series A: Math Phys Eng Sci* 2004; 460(2043): 757-780.

[28] Xiang Y, Zhu W, Deng M, et al. Experimental and numerical studies of nonlinear ultrasonic responses on plastic deformation in weld joints. *Chinese Phys B* 2015; 25(2): 024303.

[29] Zhu W , Deng M , Xiang Y , et al. Modeling of ultrasonic nonlinearities for dislocation evolution in plastically deformed materials: Simulation and experimental validation. *Ultrasonics* 2016; 68:134-141.

[30] Zhu W, Xiang Y, Liu C, et al. Fatigue damage evaluation using nonlinear Lamb Waves with quasi phase-velocity matching at low frequency. *Materials* 2018; 11(10): 1920.

[31] Wang K, Cao W, Liu M, et al. Advancing elastic wave imaging using thermal susceptibility of acoustic nonlinearity. *Int J Mech Sci* 2020; 175:105509.

[32] Stobbe D M. *Acoustoelasticity in 7075-T651 Aluminum and Dependence of Third Order Elastic Constants on Fatigue Damage*. Atlanta, GA, Georgia Institute of Technology, 2005.

[33] Yost W T and Cantrell J H. Materials characterization using acoustic nonlinearity parameters and harmonic generation: engineering materials. In: D.O. Thomposon and D.E. Chimenti (eds) *Review of progress in quantitative nondestructive evaluation*. Boston, MA: Springer, 1990,

pp.1669-1676.

[34] Wang K, Liu M, Su Z, et al. Analytical insight into “breathing” crack-induced acoustic nonlinearity with an application to quantitative evaluation of contact cracks. *Ultrasonics* 2018; 88: 157-167.

[35] Wang K, Li Y, Su Z, et al. Nonlinear aspects of “breathing” crack-disturbed plate waves: 3-D analytical modeling with experimental validation. *Int J Mech Sci* 2019; 159: 140-150.

[36] Zhao Y , Li F , Cao P , et al. Generation mechanism of nonlinear ultrasonic Lamb waves in thin plates with randomly distributed micro-cracks. *Ultrasonics* 2017; 79: 60-67.

[37] Ding X, Li F, Zhao Y, et al. Generation mechanism of nonlinear Rayleigh surface waves for randomly distributed surface micro-cracks. *Materials* 2018; 11(4): 644.

[38] Zou D, Zhen L, Zhu Y, et al. Deformed microstructure and mechanical properties of AM60B magnesium alloy under hypervelocity impact at a velocity of 4 km/s. *Mater Sci Eng. A-Struct Mater Prop Microstruct Process* 2010; 527(15): 3323-3328.

[39] Hong M , Su Z , Wang Q , et al. Modeling nonlinearities of ultrasonic waves for fatigue damage characterization: Theory, simulation, and experimental validation. *Ultrasonics* 2014; 54(3): 770-778.

[40] Zhu W, Deng M, Xiang Y, et al. Second harmonic generation of lamb wave in numerical perspective. *Chinese Phys Lett* 2016; 33(010): 71-74.

[41] de Lima W and Hamilton M. Finite-amplitude waves in isotropic elastic plates. *J Sound Vib* 2003; 265(4): 819-839.

[42] Landau L D, Lifshitz E M, Sykes J B, et al. Theory of elasticity: vol. 7 of course of theoretical physics. *Phys Today* 1960; 13: 44.

[43] Xiang Y, Deng M, and Xuan F. Creep damage characterization using nonlinear ultrasonic guided wave method: A mesoscale model. *J Appl Phys* 2014; 115: 044914.

[44] Cantrell J H . Ultrasonic investigation of the nonlinearity of fused silica for different hydroxyl-ion contents and homogeneities between 300 and 3°K. *Phys Rev B* 1978; 17(12): 4864-4870.

[45] Li W, Deng M, Xiang Y. Review on second-harmonic generation of ultrasonic guided waves in solid media (I): Theoretical analyses. *Chinese Phys B* 2017; (11): 51-65.

[46] Zhu W, Xiang Y, Liu C, et al. A feasibility study on fatigue damage evaluation using nonlinear Lamb waves with group-velocity mismatching. *Ultrasonics* 2018; 90: 18-22.

[47] Feng X, Yu S. Estimate of effective elastic moduli with microcrack interaction effects. *Theor Appl Fract Mec* 2000; 34(3): 225-233.

[48] Zhao Y, Qiu Y, Jacobs L J, et al. A micromechanics model for the acoustic nonlinearity parameter in solids with distributed microcracks. In: *AIP Conf Proc* 2016; pp. 060001.

[49] Rose J L. *Ultrasonic guided waves in solid media*, Cambridge University Press, Cambridge, 2014. ISBN: 978-1-107-04895-9.